Moist Convection at a Surface Cold Front

N. ANDREW CROOK

Geophysical Fluid Dynamics Program, Princeton University, Princeton, NJ 08542

(Manuscript received 3 February 1987, in final form 5 June 1987)

ABSTRACT

The motion of a surface cold front in an environment that is unstable to moist convection is studied with the aid of both hydrostatic and nonhydrostatic two-dimensional models. Simulations with the hydrostatic model essentially extend the work reported by Ross and Orlanski. It is shown that when deep convection occurs, Coriolis turning of the flow into the convective line creates a poleward low-level jet ahead of the front. It is also shown that after the generation and decay of the first convective element, another line develops on the order of a day later. It is found that the intensity of this line increases significantly if a north–south gradient of moisture is specified.

The periodicity in convective activity at the front is explained in terms of an inertial gravity oscillation in the low-level convergence. The first convective system, which decays when the subcloud layer is dried out by the convection, forces a geostrophic imbalance in the surface front and the surrounding environment. In returning to geostrophic balance after the decay of the first system, the front and surrounding environment tend to oscillate as inertial gravity waves propagate away from the region of imbalance. It is shown that the convergence at low levels ahead of the front oscillates with a period of approximately 12 hours and that ascent returns to the frontal zone 6 hours after the decay of the first system. The second system then develops when this low-level convergence destabilizes the atmosphere. The discrepancy between the inertial gravity wave period and the period between convective line generation obtained in the hydrostatic model (20–27 h) is explained by the crude representation of moist convection in the hydrostatic, filtered model. A nonhydrostatic model with horizontal resolution of 2.8 km is used to study the same system and a periodicity in convective activity is again found, this time with the second system commencing some 7 hours after the decay of the first.

Finally, observations of cold fronts in the Midwest of the United States are analyzed to explore the importance of convective oscillations in the motion of surface cold fronts.

1. Introduction

The dynamical processes that occur in the region of a cold front have been studied extensively (for recent reviews see Hoskins, 1982; Orlanski et al., 1985), primarily because a large proportion of severe weather occurs in these regions. Most of these studies have concentrated on the properties of the frontal circulation in the absence of moisture in either a quasi-geostrophic, semigeostrophic or, more recently, primitive equation setting. The reason that moist frontal processes have not yet been extensively studied is largely because moist convection occurs on a vastly different scale (~1–10 km) to that of the front itself. Nevertheless, some recent studies (Ross and Orlanski, 1978; Hsie et al., 1984; and Mak and Bannon, 1984) have begun to address this complicated problem.

In the present study we examine some of the effects of moist convection on the frontal circulation with the aid of a two-dimensional numerical model of an idealized surface front. This study essentially extends that of Ross and Orlanski (1978), which used a hydrostatic numerical model with a horizontal resolution of 20 km. In Ross and Orlanski (1978) a large convective system (with a width of ~200 km) grew in the ascending air ahead of the front, moved slowly ahead and then decayed. The time scale of the convection was of the order of 10 hours. In the present study it is shown that this behavior of generation, forward propagation, and then decay can occur a number of times in the lifetime of a front.

The same frontal processes are also studied with a higher-resolution (Δx = 2.8 km) nonhydrostatic numerical model. In these simulations, in which convection is modeled more accurately than in the hydrostatic model, a periodicity to the convective activity is also found, this time with the second system developing some 7 hours after the first.

2. Simulations with hydrostatic numerical model

a. Description of model and initial fields

The numerical model that is used in the first half of this study is similar to that described in Orlanski and Ross (1977), (with the inclusion of moisture variables discussed in Ross and Orlanski, 1978) with the following exceptions:

(i) The horizontal gridlength is reduced to 14 km. A slightly different coordinate stretching in the vertical is used with Δz = 200 m at the ground, increasing to

450 m at the top of the model (which is at height of 14 900 m).

(ii) A damping layer is used above 10.5 km. The damping layer is similar to that described in Crook (1986) with the exception that the damping time decreases to 20 minutes at the top of the domain.

(iii) The model is initialized with a cross-front circulation. In Ross and Orlanski (1978) this circulation, which was not present at $t = 0$, was allowed to evolve during the simulation. It consequently took some time before the circulation settled into a quasi-steady state, as inertial gravity waves propagated away from the frontal region.

The cross-front circulation is obtained by solving Eq. 4.11 of Orlanski and Ross (1977), which is a version of the Sawyer-Eliassen equation.

$$N^2\frac{\partial^2\psi'}{\partial x^2}+f\left(f+\frac{\partial v}{\partial x}\right)\frac{\partial^2\psi'}{\partial z^2}-2f\frac{\partial v}{\partial z}\frac{\partial^2\psi'}{\partial x\partial z}=-2f\frac{\partial v}{\partial x}\frac{\partial U_g}{\partial z} \quad (1)$$

where

$$\psi'=\psi-\psi_0(z), \quad U_g=\frac{\partial\psi_0}{\partial z}$$

(as we have set $\alpha_0 = 1$).

Equation 1 is elliptic as long as the potential vorticity

$$q=N^2f\left(f+\frac{\partial v}{\partial x}\right)-\left(f\frac{\partial v}{\partial z}\right)^2$$

is everywhere positive. In the initial fields that are used in this study there are small regions of negative potential vorticity at the lower boundary, which means that Eq. 1 cannot be solved by conventional methods. To obtain an approximate solution for the use in initialization, we first solve the quasi-geostrophic form of Eq. (1)

$$N^2\frac{\partial^2\psi'_{QG}}{\partial x^2}+f^2\frac{\partial^2\psi'_{QG}}{\partial z^2}=-2f\frac{\partial v}{\partial x}\frac{\partial U_g}{\partial z} \quad (2)$$

with the condition that the disturbance vanishes at the boundaries (i.e., $\psi'_{QG} = 0.0$).

We then assume that the streamfunction ψ' can be written as $\psi'_{QG} + \psi''$ (where ψ'' is small compared with ψ'_{QG}). The correction term ψ'' can then be obtained by substituting into Eq. 1, which gives

$$N^2\frac{\partial^2\psi''}{\partial x'}+f\left(f+\frac{\partial v}{\partial x}\right)\frac{\partial^2\psi''}{\partial z^2}=2f\frac{\partial v}{\partial z}\frac{\partial^2\psi'_{QG}}{\partial x\partial z}-f\frac{\partial v}{\partial x}\frac{\partial^2\psi'_{QG}}{\partial z^2}. \quad (3)$$

In this way, the equations that are solved are always elliptic. In practice, it was found that the magnitude of ψ'' was always less than 15% of ψ'_{QG}.

It should be noted that in all of the simulations studied there was no sign of an unstable disturbance similar to symmetric instability in the small region of negative potential vorticity at the lower boundary. This layer of negative potential vorticity arises because we have not included surface friction at the lower boundary. At $t = 0$, the front is in thermal wind balance at the lower boundary and thus the term $f\partial v/\partial z$ must be large to balance the horizontal temperature gradient $(g/g_0)\partial g/\partial x$. However, in the real atmosphere surface friction also balances the horizontal temperature gradient, allowing the term $f\partial v/\partial z$ to fall below its geostrophic value (for example, see Palmen and Newton, 1969, p263).

(iv) The initial v field (and the θ field that balances it) are similar to the surface jet case (SJ2) examined in Orlanski and Ross (1977). One important difference, however, is that the north–south velocity in their study vanishes at the western boundary whereas there exists a region of constant (in x) north–south velocity in the present study which extends all the way to the western boundary. The analytical form of the v field is given in Eq. 4:

$$v(x,z)=v_{\text{back}}+v_{\text{front}}*\text{shape}(x,z) \quad (4)$$

where

$$\text{shape}(x,z)=\exp-\left(\frac{x-x_0}{x_L}\right)^2\left[1+\tanh\left(\frac{z_0-z}{z_H}\right)\right]\Big/\left[1+\tanh\left(\frac{z_0}{z_H}\right)\right] \quad \text{for} \quad x>x_0$$

$$\text{shape}(x,z)=\text{shape}(x_0,z) \quad \text{for} \quad x<x_0.$$

For the first simulation the parameters in Eq. (4) are set as follows:

$$v_{\text{front}}=35.0\,\text{m s}^{-1}$$

$$v_{\text{back}}=0.0\,\text{m s}^{-1}$$

$$x_L=158.0\,\text{km}$$

$$x_0=305.0\,\text{km}$$

$$z_0=-400.0\,\text{m}$$

$$z_H=1800.0\,\text{m}.$$

The east–west synoptic wind $U_g(z)$ is chosen so that the front is quasi-stationary in the domain. In the first simulation $U_g(z)$ takes the form

$$U_g(z)=-4.9\,\text{m s}^{-1}+15.0\,\text{m s}^{-1}\tanh(z/7000\,\text{m}).$$

Thus there is only a weak vertical shear of 15 m s^{-1} across the model domain. A geostrophic temperature field $\theta_g(y, z)$ balances this vertical shear according to the thermal wind relation

$$\frac{\partial\theta_g[1+0.61q]}{\partial y}=\frac{\partial\theta_{vg}}{\partial y}=-\frac{f\theta_{v0}}{g}\frac{\partial U_g}{\partial z} \quad (5)$$

where the subscript v denotes virtual potential temp.

For the flow to be two-dimensional

$$\frac{\partial \theta_{vg}}{\partial z} = -\frac{f\theta_{v0}}{g} y \frac{\partial^2 U_g}{\partial z^2}$$

must be small compared with $\partial\theta/\partial z$ ($\theta_{vg} = 0$ at $y = 0$). As shown in Orlanski (1986) this relation is equivalent to $L_y < N^2/fU_{gzz}$ where L_y is the meridional scale of the disturbance which can be set equal to a typical advection velocity multiplied by the disturbance time scale. Using the parameters of the present study $L_y < 6000$ km, which is certainly satisfied for the disturbance under study.

As in Orlanski and Ross (1977), $\theta(z)$ is specified on the right-hand boundary and the thermal wind equation is used to specify the potential temperature throughout the domain. For the first simulation the lapse rate at the right-hand boundary is 2.0×10^{-3} °C m^{-1} for $z < 4.0$ km, 4.0×10^{-3} °C m^{-1} for 4.0 km $< z <$ 10.0 km, and 14.5×10^{-3} °C m^{-1} for $z > 10$ km.

Figure 1 shows the initial v field, the θ and θ' field that balances it and the cross-front circulation ψ' (θ' and ψ' are the deviations from the initial θ_0 and ψ_0 fields, respectively). The center of the circulation is located just behind the leading edge of the front (about 15 km behind the surface position of the $\theta' = -2.0$°C contour). This is the region where the forcing term

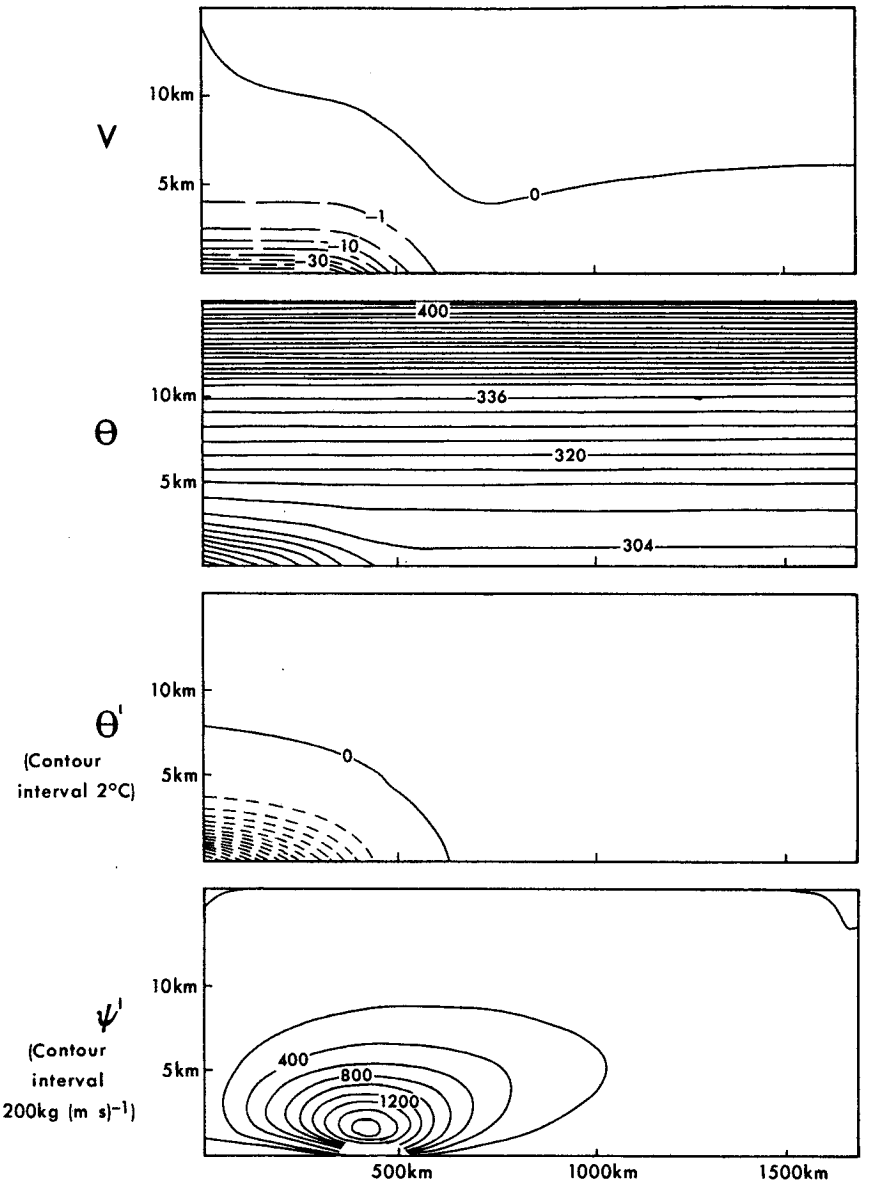

FIG. 1. The initial fields of (a) north–south velocity component v, (b) potential temperature θ, (c) perturbation potential temperature θ' and (d) perturbation stream function ψ'.

$$-2f\frac{\partial v}{\partial x}\frac{\partial U_g}{\partial z}$$

on the right-hand side of Eq. 1 reaches its maximum value. Since $\partial v/\partial x$ is set to zero in the region of the left-hand boundary there is no forcing there. Tests were performed to determine if the position of the forcing maximum relative to the left-hand boundary (controlled essentially by the parameter x_0) affected the initial circulation. These tests showed that as long as x_0 was greater than about 100.0 km, the circulation was largely unaffected. (In section 2c tests will be performed to check if the lateral boundaries have any effect on the moist convective flow.)

The maximum horizontal temperature gradient at the surface is 7°C/100 km. This is consistent with the observed gradients in summertime cold fronts in southeast Australia (see Ryan and Wilson, 1985) and the surface cold front during SESAME-AVE III studied by Ogura and Portis (1982), although significantly less than the 10°C in 18 km observed by Sanders (1955) for an intense surface front in the Midwest.

The initial cross-front circulation gives a maximum vertical velocity of 0.7 cm s^{-1} or 25 m h^{-1} just ahead of the surface front. This is a rather weak vertical motion compared to that often observed in frontal regions and to that obtained in similar numerical models (see Keyser and Anthes, 1986). A few comments can be made on this discrepancy. First, we are only interested here in the circulation forced by a surface front. In the studies of Keyser and Anthes (1982) and Reeder and Smith (1986), for example, the front extends through the whole troposphere and thus provides a much deeper forcing to the vertical motion ahead of the front. Second, it has been shown by Keyser and Anthes (1982) that surface friction, which is not included in the present study, can increase the vertical motion, although in their study the vertical motion was increased only by about 25%. Third, Mak and Bannon (1984) suggest that moist processes can provide a steady forcing to the flow ahead of the front and hence increase the vertical motion there. It should also be noted that we find in the present study of fronts in convective environments that the circulation is rarely steady and, in fact, an inertial-gravity oscillation, with vertical velocities significantly larger than those in the steady circulation, is forced by the convection.

To test the initial steadiness of the frontal circulation the numerical model (with moisture excluded) was integrated forward in time for 26 hours. The maximum vertical velocity is plotted as a function of time in Fig. 2. There is a small rise of about 20% in the first 5 h, but after that the vertical velocity stays fairly constant at a value of 0.67 cm s^{-1}. Also plotted is the maximum vertical velocity in the frontal region for a simulation without the cross-front circulation included at $t = 0$. As can be seen, the vertical velocity oscillates with a period which is very close to 12 h. This oscillatory behavior of the front as it moves towards geostrophic balance is very important for the generation of convection at the front, as will be shown later.

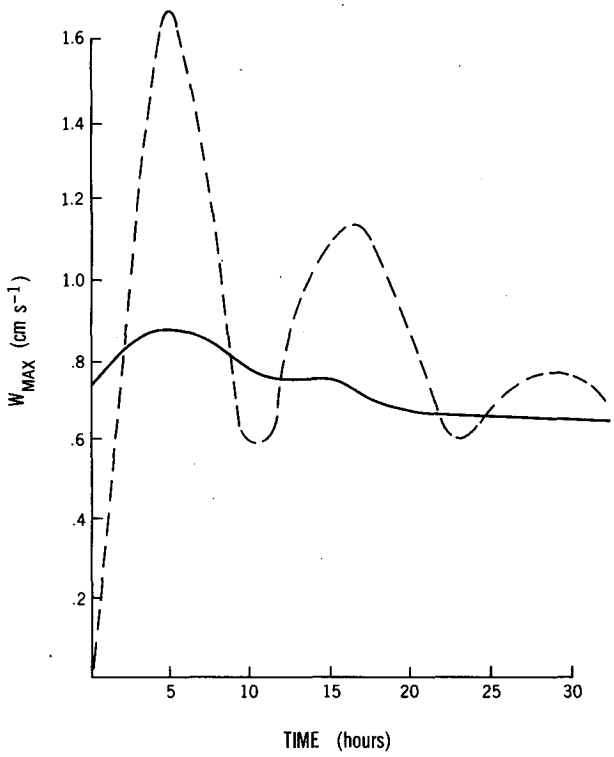

FIG. 2. Maximum vertical velocity against time for a dry front. The solid line is for a simulation which commences with the cross-front circulation shown in Fig. 1d, the dashed line is for a simulation with no initial circulation.

The relative steadiness of the fields when the cross-front circulation is included allows the specification of a moisture field at the beginning of the simulation. This is in contrast to the study of Ross and Orlanski (1978) in which the model was integrated to a steady state before the inclusion of moisture. This was necessary to exclude the possibility of the initial unsteadiness generating convection; however, the inclusion of moisture affects the virtual potential temperature field, and this can lead to an unrealistic modification of the frontal circulation.

As in Ross and Orlanski (1978) we allow the frontal circulation to determine the scale of the convection. This is in contrast to the majority of studies on convection in which the convection is initiated by an anomalous heating or cooling. As length and time scales have to be specified a priori for this heating or cooling it is possible that these scales may influence the scale of the convection that is initiated. It will be shown, especially in the high-resolution model, that convection commences in a much more realistic manner when frontal convergence alone is allowed to produce saturation.

Furthermore, as in Ross and Orlanski (1978), saturation occurs when the mixing ratio q exceeds kq_s where q_s is the saturation mixing ratio and k is set to 0.95. The factor k is included to represent the fact that the mixing ratio q at each grid point is averaged over a 14-km wide box and begins to condense when the average relativity humidity over the box is less than 100%. Sensitivity tests showed that the results are largely independent of k as long as the difference between k and the initial relative humidity profile is kept constant.

The simulations to be discussed (both with the hydrostatic and nonhydrostatic model) are summarized in Table 1.

b. Results

All of the simulations to be discussed are initialized with a relative humidity profile which is constant in x and a piecewise linear function in z. In the first simulation (run 1) the relative humidity at $z = 0$ is 55% increasing to a maximum at $z = 2200$ m of 84% (the relative humidity at this point is denoted Rh2), then decreasing to 5% at the top of the domain. This is similar to that observed ahead of the squall lines studied by Ogura and Chen (1977) (45% at the ground, increasing to 80% at 800 mb) and Ogura and Liou (50% at the ground, 75% at 800 mb). The slightly increased values of relative humidity in the numerical simulation allow an earlier development of convection and a subsequent decrease in computer time needed to simulate the full lifetime of the convection.

Figure 3 indicates the development of convection ahead of the front (the θ' field is shown in Fig. 3a; the streamlines in a frame of reference in which the convection is at rest are plotted in Fig. 3b). Cloud first appears at $t = 10$ hours in the ascending branch of the circulation at a height of about 3.2 km (above the relative humidity maximum, $z = 2200$ m, and the level of maximum vertical velocity, $z = 1400$ m). This cloud grows upward slowly, with a peak in vertical velocity of 1.5 m s^{-1} at $t = 28$ hours. As discussed in Ross and Orlanski (1978) the low horizontal resolution ($\Delta x = 14.0$ km) makes it impossible to resolve the intense updrafts (with widths $\sim$1 km and vertical velocities $\sim$10 m s^{-1}) that are observed in strong cumulonimbus. Thus the low vertical velocities obtained in the model result in the convection growing much more slowly than occurs in the real atmosphere. As will be described later, a high-resolution model ($\Delta x = 2.8$ km) of the same system has been integrated and shows the convection developing in a much more realistic manner.

TABLE 1. Summary of numerical simulations

Run 1	Rh2 = .84 x_L = 158 km x_0 = 305 km
Run 2	As in run 1 except with north–south gradient of moisture specified.
Run 3	Same as run 2 except with frontal zone moved 120 km east
Run 4	Same as run 2 except with frontal zone moved 120 km west
Run 5	Same as run 1 except with Rh2 = 0.79
Run 6	Same as run 1 except with Rh2= 0.945
Run 7	Same as run 1 except with frontal width decreased by 0.7
Run 8	Same as run 1 except with frontal width decreased by 0.5
Run 9	Simulation with nonhydrostatic model Rh2 = 0.995
Run 10	Same as run 9 except with precipitation scheme from hydrostatic model.

As the cloud grows it moves into the upper-level westerlies that deflect the convection eastward. The convection thus moves ahead of the surface front. At about the same time ($t = 33$ h) the convective line begins to decay. In Fig. 4 the maximum vertical velocity in the domain is plotted as a function of time. Also plotted in Fig. 4 is the speed of the leading edge of the front (in this case, defined by the surface position of the $\theta' = -2$°C contour). This shows that the front is not completely stationary, but moves forward slowly as the convection grows and recedes as the convection decays. As will be shown in section 2f this oscillation in the velocity of the surface front, although seemingly rather small, is very important for the further development of convection ahead of the front.

The difference between the θ' field from the moist simulation and a dry simulation at the same time ($t = 31.1$ h) is plotted in Fig. 5(a). In Fig. 5(b) the difference in the v fields is plotted. To avoid any discrepancy being introduced by a change in virtual potential temperature, the dry simulation uses the same relative humidity field as the moist simulation, with the only difference being that condensation is not allowed to occur (i.e., the air is allowed to become supersaturated). The $\Delta\theta'$ field shows that convection has warmed the middle troposphere (by the release of latent heat in the convective system and by subsidence warming outside the convection) and cooled a region around 300 mb at the top of the convective line (by lifting and by the evaporation of cloud water). The negative contour at the leading edge of the surface front indicates that the moist front has moved forward relative to the dry front. This increased velocity of the moist front is also shown by the negative contours of Δv in the region of the front itself.

Southerly motion has been induced ahead of the front by the convection. A jet of 10 m s^{-1} is located at about 750 mb, and is indicated by an arrow in Fig. 5(b). This jet is caused by the Coriolis turning of flow into the convective element on its eastern flank. A similar northerly jet of about 9 m s^{-1} can be seen to the west of the southerly jet and is caused by the turning of the flow into the western flank. Similarly aloft, centered about 400 mb, is a northerly jet (southerly jet) caused by the deflection of the outflow on the eastern (western) side of the convection.

A low-level poleward jet is a common feature in both observations of surface fronts and in numerical models. Browning and Harold (1970) observed a southerly jet

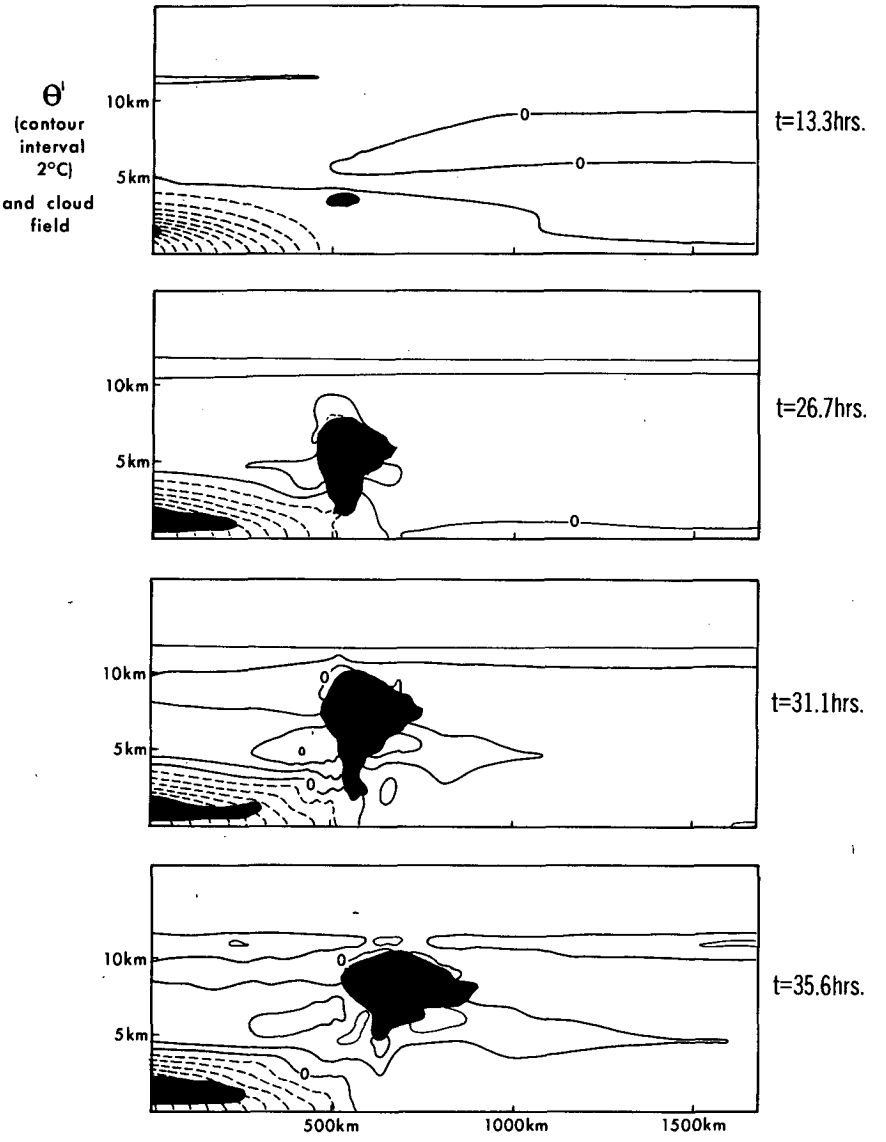

FIG. 3a. Perturbation potential temperature field for run 1 (contour interval 2°C). Cloud is indicated by the shaded regions.

of about 15 m s^{-1} ahead of a front crossing the British Isles. This jet was located below 1 km, which was also the level of flow into the convection ahead of the front. In a numerical model of the cold front of 26 April 1979 (SESAME-AVE III) Orlanski et al. (1985) obtained a southerly jet of velocity 13 m s^{-1} at a height of about 1.5 km (see their Fig. 6). Again, this jet is coincident with the level of inflow for the convection in the frontal region. In a recent study in southeastern Australia, this poleward flow ahead of the front was a commonly observed feature, although its strength and position showed significant variability (Ryan and Wilson, 1985).

The poleward jet evident in Fig. 5(b) results in an increase in the potential temperature at this level. For a 10 m s^{-1} jet over 24 hours this increase is approximately 4°C. This increase tends to destabilize the air above this level which has important implications for the long-term development of the system. At t = 40 hours after the first convective element has essentially decayed, a further convective line begins to grow above the surface front. The development of this second line is depicted in Fig. 6(a) and (b) and the maximum vertical velocity plotted in Fig. 4. The interval between the time of maximum convective activity is about 27 h, as can be seen from Fig. 4. Also, the second squall line is slightly more intense than the first, which is most likely due to the destabilization of the atmosphere by the differential advection of potential temperature in the poleward jet.

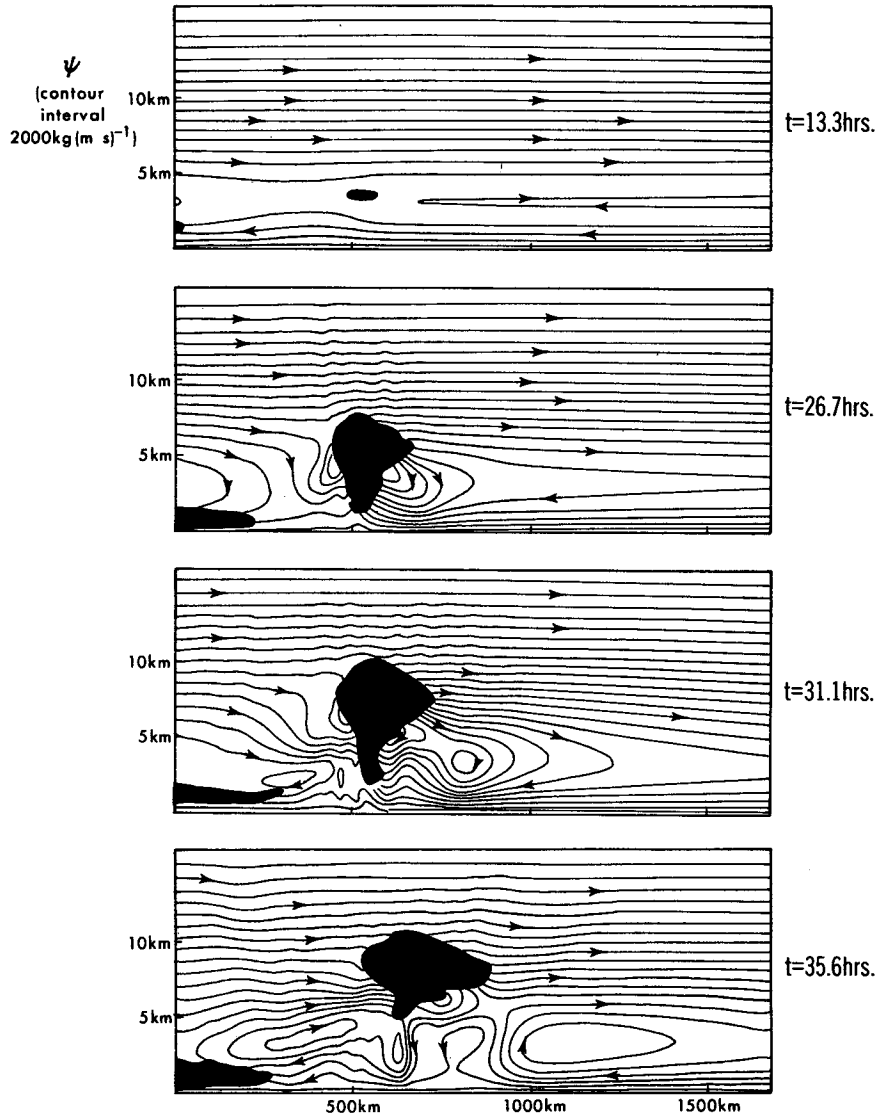

FIG. 3b. Streamfunction in a frame of reference in which the convective system is at rest.

Figure 6(a) shows that a large area of cloud has begun to form behind the surface front. This cloud formation, which essentially results from the fact that we have specified a north–south temperature gradient but no moisture gradient in that direction, can be elucidated in the following manner. Let us assume that there is a point at the surface in the cold-frontal air where the potential temperature is constant with time, i.e., $\partial\theta/\partial t = 0.0$. Since the vertical advection vanishes at the surface there must be a balance between the advection of warm air from the east (the $u\partial\theta/\partial x$ term) and the advection of cold air from the north (the $v\partial\theta_g/\partial y$ term), neglecting diabatic processes for the moment. However, on examination of the mixing ratio equation (Eq. (2.6) in Ross and Orlanski, 1978) it is clear that there is advection of moister air from the east, i.e., the $u\partial q/\partial x$ term, but no advection in the north–south direction. Thus, the relative humidity at this surface point will increase since q is increasing while θ remains constant. Hence, after a sufficient length of time, cloud will form in the surface cold front.

The fact that we have specified a $\partial\theta_g/\partial y$ but no $\partial q/\partial y$ means that there is an implied north–south gradient of relative humidity. This can be viewed as a slight inconsistency in the two-dimensional assumption of the model. To circumvent this problem a gradient in q can be specified in the north–south direction. Although the introduction of a $\partial q/\partial y$ term does present problems of its own (as will be discussed presently), it gives a useful insight into the importance of the low-level poleward jet in supplying moisture into the convective system.

In the model the saturation mixing ratio, q_s, is given by

$$q_s = q_{s0} \exp\left(\frac{L\Pi_0}{R_v T_0^2}\theta'\right) \tag{6}$$

where the quantities with the subscript "0" are mean state variables.

In the y direction, the variation of potential temperature is given solely by the term $\theta_g(y, z)$. Hence, for the base state

$$q_s(y, z) = q_{s0} \exp\left[\frac{L\Pi_0}{R_v T_0^2}\theta_g(y, z)\right]. \tag{7}$$

As already stated, the initial mixing-ratio field is taken so that the relative humidity is only a function of z, say $R(z)$. If we define the initial base-state mixing ratio as $q_0(z) + q_g(y, z)$ (where $q_g \equiv 0$ at $y = 0$) and require that the relative humidity be constant in y, we then have

$$q_0(z) + q_g(y, z) = R(z)q_s(y, z)$$
$$= R(z)q_{s0} \exp\left[\frac{L\Pi_0}{R_v T_0^2}\theta_g(y, z)\right].$$

Taking the derivative in the y direction we obtain

$$\frac{\partial q_\theta}{\partial y} = R(z)q_{s0}\frac{L\Pi_0}{R_v T_0^2} \exp\left[\frac{L\Pi_0}{R_v T_0^2}\theta_g(y, z)\right]\frac{\partial \theta_g}{\partial y}$$
$$= q(z)\frac{L\Pi_0}{R_v T_0^2}\frac{\partial \theta_g}{\partial y} \quad \text{at} \quad y = 0 \tag{8}$$

If we specify a gradient in q in the north–south direction from Eq. (8), the relative humidity of the base state will be constant in y. A slight problem arises in deciding the correct choice for the base state of q, since the mixing ratio varies by a factor of 3 across the front at $z = 0$. In the simulation described below we choose the base state as that ahead of the front, since we are primarily interested in the advection of moisture by the poleward flow ahead of the front. This poleward flux of moisture is known to be especially important in maintaining the severe convective lines that occur ahead of fronts in the Midwest of the United States, where warm, southerly winds bring moisture from the Gulf of Mexico.

The model was run with exactly the same conditions as before, except with a north–south gradient of q specified (run 2). The maximum vertical velocity is plotted against time for both run 1 and run 2 in Fig. 7. As can be seen, the first convective system in the two simulations are approximately the same. (The system in run 2 is slightly weaker and occurs later than in run 1, which is due to the fact that the first system develops in a slight northerly flow, of about 0.5 m s^{-1}, and this reduces q in run 2 relative to run 1.) However, after the first line has been generated, the poleward jet that develops advects moisture into the plane of the simulation and makes the atmosphere in that region more convectively unstable. The second system in run 2 is 30% more intense (in terms of vertical velocity) than in run 1. Furthermore, the time period between convective systems is reduced in run 2 to a value of 20 hours (compared to 27 h in run 1).

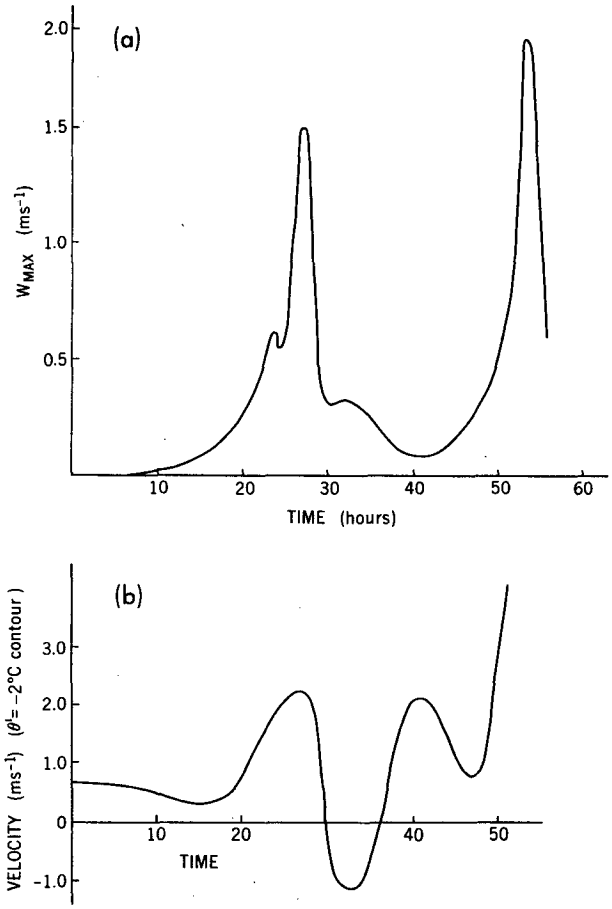

FIG. 4. (a) Maximum vertical velocity plotted against time for run 1. (b) The speed of the surface front as defined by the surface position of $\theta' = -2$°C contour.

c. *Sensitivity to lateral boundaries*

In this section we shall examine the sensitivity of the flow to the lateral boundaries by placing the frontal zone in different positions in the model domain. In section 2f it will be shown that the periodicity in convective activity crucially depends on an inertial gravity oscillation in the frontal zone; thus, to obtain the periodicity in convection it is important that a significant portion of the frontal zone is included in the model domain.

The sensitivity tests are performed for run 2 (north–south gradient of q specified), since there is no difficulty with cloud forming at the left-hand boundary. The maximum vertical velocity is plotted in Fig. 8 for three

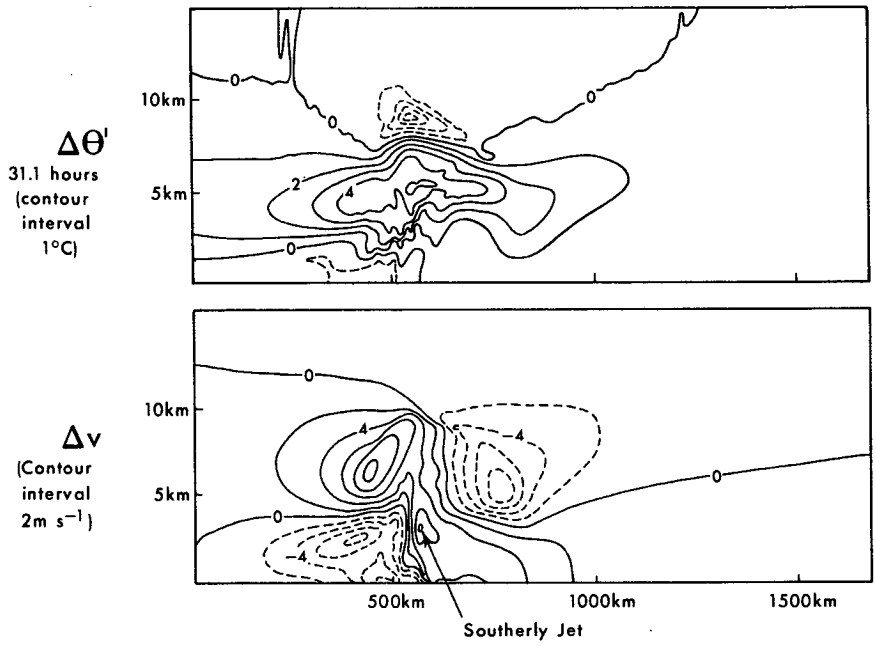

FIG. 5. (a) Difference in θ' between moist and dry simulations at $t = 31.1$ h. (b) Difference in v between moist and dry simulations at $t = 31.1$ h. The arrow indicates the poleward jet induced by the low-level flow into the eastern flank of the convective system.

simulations with different x_0 (which determines the position of the frontal zone). Run 2 is indicated by the dashed line, the solid line (run 3) is for a simulation with the frontal zone moved 120 km east, i.e., further from the left-hand boundary, and the dotted line (run 4) is plotted for a simulation with the frontal zone moved 120 km to the west. As can be seen, the periodicity in convection occurs in all three simulations, with little apparent difference between runs 2 and 3 in which the frontal zone is a significant distance from the left-hand boundary. Run 4 is somewhat different in that the maximum vertical velocity is slightly less and occurs later than in the other two simulations. It was also found that if the low-level easterly flow specified at $t = 0$ was too strong, so that the frontal zone moved close to the western boundary, then the second convective system failed to develop. This is consistent with the theory, to be discussed in section 2f, that the second line develops when the first system forces the front out of geostrophic balance. Hence a sufficient portion of the frontal zone must be included in the model domain if the second system is to develop.

d. Heat and moisture budgets in the flow

Run 2 indicates that the north–south flow is important in supplying heat and moisture to the convection. We can examine this process in more detail by calculating budgets in the convective region. If we ignore diabatic effects, the potential temperature satisfies the following budget equation:

$$\frac{\partial}{\partial t}\int_{z_1}^{z_2}\int_{x_1}^{x_2}\rho_0\theta\,dx\,dz+\int_{z_1}^{z_2}[\rho_0 u\theta]_{x_1}^{x_2}dz+\int_{x_1}^{x_2}[\rho_0 w\theta]_{z_1}^{z_2}dx+\int_{z_1}^{z_2}\int_{x_1}^{x_2}\rho_0 v\frac{\partial\theta_g}{\partial y}dx\,dz=0 \quad (9)$$

where the budget is taken over a cuboid of unit width in the y direction and stretching from x_1 to x_2 (in the east–west direction) and z_1 to z_2 in the vertical. The mixing ratio q also satisfies the same equation as long as there is no condensation or evaporation; also for run 1, the last term is zero as $\partial q_g/\partial y \equiv 0$. The rate of change of θ and q in the control volume will be expressed as the sum of two terms 1) convergence in the cross-front direction and 2) flux in the north–south direction. Equation 9 is rewritten as

$$\frac{\partial\bar{\theta}}{\partial t}=\underset{\substack{\text{convergence in}\\ \text{cross front direction}}}{F(\theta)_{xz}}+\underset{\substack{\text{flux in the}\\ \text{north–south direction}}}{F(\theta)_y} \quad (10)$$

$$\bar{\theta}=\int_{z_1}^{z_2}\int_{x_1}^{x_2}\rho_0\theta\,dx\,dz/\bar{\rho}_0$$

$$F(\theta)_{xz}=-\left(\int_{z_1}^{z_2}[\rho_0 u\theta]_{x=x_1}^{x_2}dz+\int_{x_1}^{x_2}[\rho_0 w\theta]_{z=z_1}^{z_2}dx\right)$$

$$\bar{\rho}_0=\int_{z_1}^{z_2}\int_{x_1}^{x_2}\rho_0\,dx\,dz$$

$$F(\theta)_y=-\left(\int_{z_1}^{z_2}\int_{x_1}^{x_2}\rho_0 v\frac{\partial\theta_g}{\partial y}dx\,dz\right)\Big/\bar{\rho}_0.$$

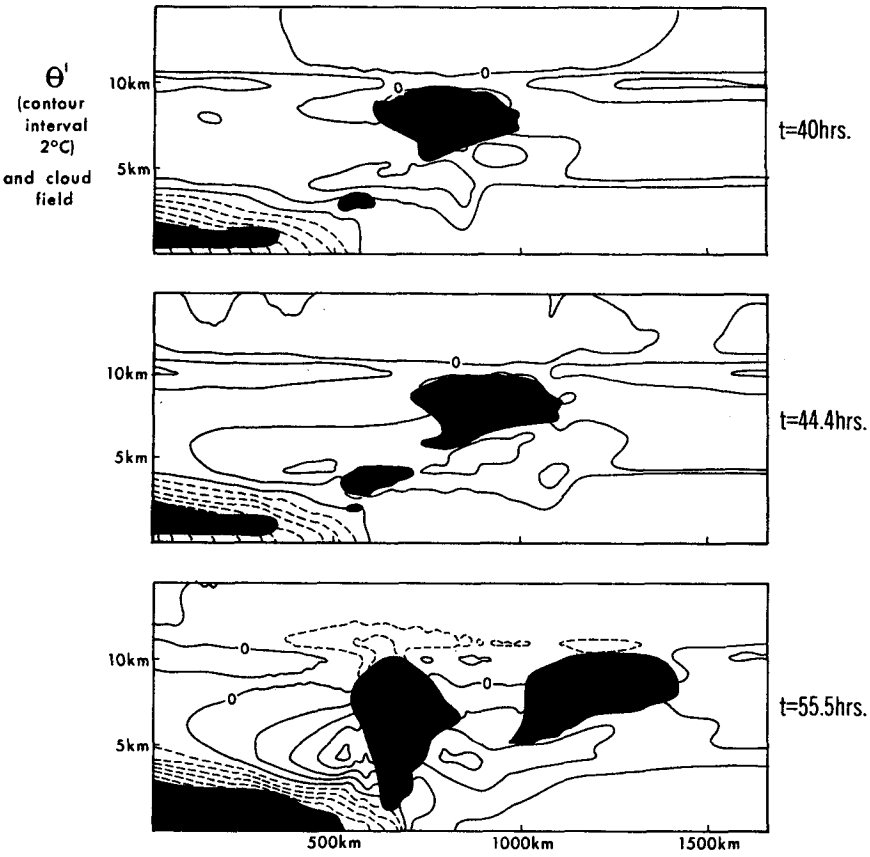

FIG. 6. The further development of run 1. (a) The θ' field with cloudy regions shaded. Note the development of low-level cloud in the frontal region.

The budget will be taken over a cuboid, located at the position where the first convective line begins to develop (which, because of the stationarity of the front, is very close to the generation position of the second line). A schematic is given in Fig. 9. Budgets will be calculated essentially at two times: first, just before the first cloud develops and, second, after the first convective line has propagated clear of the budget box and just before the second line appears. The budgets are also time-averaged over a period of 2 hours.

The fluxes of θ and q just before the first cloud develops and then just before the development of the second line for run 1 are indicated in Table 2.

There are several points to note about Table 2. First, as a consistency check, the initial cooling rate of -0.9°C day^{-1} due to cross-front circulation along with the specified lapse rate of 2°C km^{-1} in the lowest 4 km gives a mean vertical motion of 22 m h^{-1} in the budget box (recalling that the maximum vertical velocity is 25 m h^{-1}). Furthermore, prior to the generation of the second line, the heating due to the north–south velocity of 3.5°C day^{-1} is consistent with the specified potential temperature gradient $\partial\theta_g/\partial y$ and the poleward velocities of $\sim$10 m s^{-1} ahead of the front.

An important point to note about Table 2 is that the circulation is substantially more intense before the second cloud develops than before the first. This can be seen quite clearly in Fig. 6(b) at t = 40 h, and indicates that the second convective line develops before the front has time to return to the balanced, steady state that exists at the start of the simulation. This is consistent with the theory that will be discussed in section 2e, that the second line is generated primarily by an oscillation in the low-level convergence that is forced by the first line.

We can examine the change in relative humidity in the box in the following manner:

$$\frac{\partial}{\partial t}\frac{q}{q_s} = q\frac{\partial}{\partial t}\frac{1}{q_s} + \frac{1}{q_s}\frac{\partial q}{\partial t}$$

$$\frac{\partial}{\partial t}\frac{q}{q_s} = \frac{-L\Pi_0}{R_v T_0^2}\frac{q}{q_s}\frac{\partial\theta'}{\partial t} + \frac{1}{q_s}\frac{\partial q}{\partial t}$$

$$\therefore \frac{1}{(\mathrm{Rh})}\frac{\partial(\mathrm{Rh})}{\partial t} = \frac{-L\Pi_0}{R_v T_0^2}\frac{\partial\theta'}{\partial t} + \frac{1}{q}\frac{\partial q}{\partial t} \qquad (11)$$

where

$$\mathrm{Rh} = q/q_s.$$

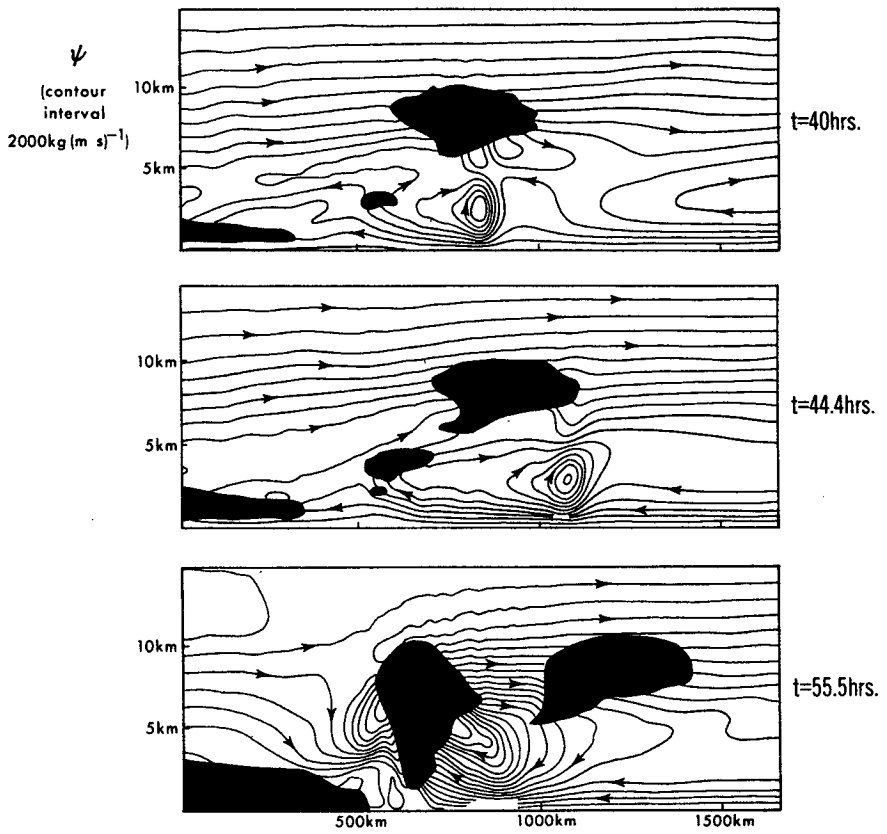

FIG. 6. (*Continued*) (b) Streamfunction in a frame of reference in which the *second system* is at *rest*.

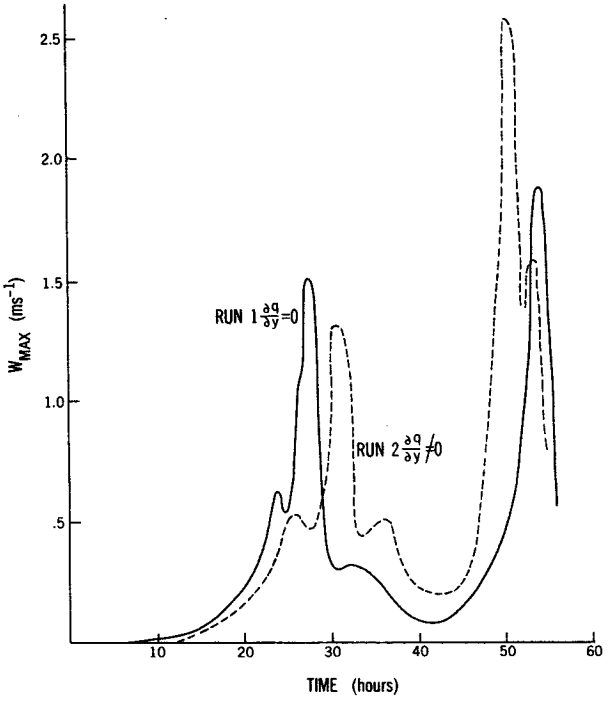

FIG. 7. Maximum vertical velocity against time for run 2 (with a north–south gradient of moisture specified) and run 1.

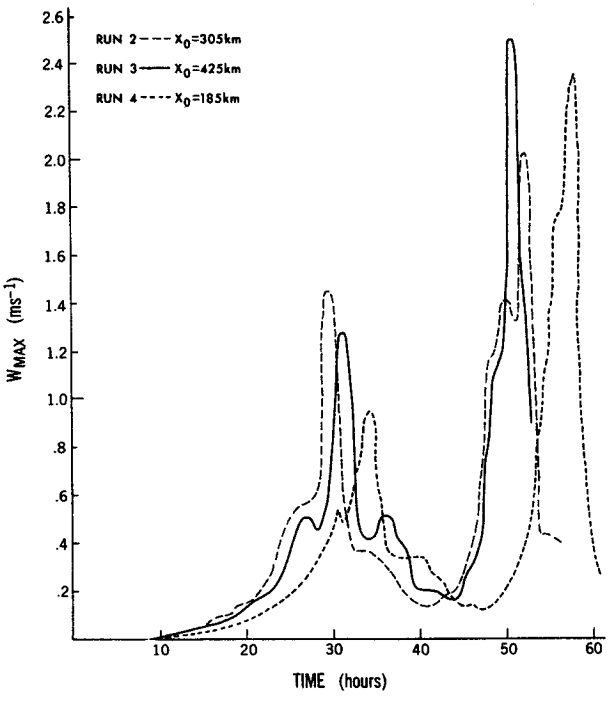

FIG. 8. Maximum vertical velocity for three simulations with different initial positions of the frontal zone in the model domain.

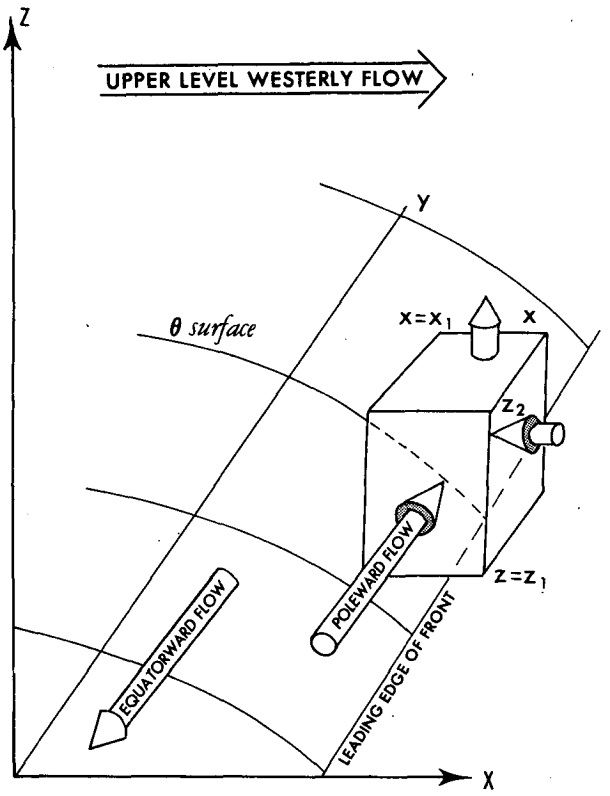

FIG. 9. Schematic of frontal zone showing cuboid ahead of front for the purpose of budget calculations.

The same equation holds approximately for the average q and θ' in the budget box $\bar{q}$ and $\bar{\theta}'$ (as long as the variation in q_{s0} is small). Thus we can write

$$\frac{1}{\overline{\mathrm{Rh}}}\frac{\partial\overline{\mathrm{Rh}}}{\partial t} \approx -\frac{\overline{L\Pi_0}}{R_v T_0^2}\frac{\partial\bar{\theta}'}{\partial t}+\frac{1}{\bar{q}}\frac{\partial\bar{q}}{\partial t} \equiv D\theta' + Dq.$$

The increase in relative humidity in the box is due to both an increase in q and a decrease in potential temperature (and hence saturated mixing ratio).

Before the first line is generated we have

$$D\theta' = 0.24\%\ \mathrm{h}^{-1} \quad Dq = 0.56\%\ \mathrm{h}^{-1}$$

The sum $D\theta' + Dq = 0.8\%\ \mathrm{h}^{-1}$ is consistent with the maximum rate of increase in the cuboid of $1.0\%\ \mathrm{h}^{-1}$.

For the time period before the second line is generated we can separate $D\theta'$ into that due to the cross-frontal circulation $D\theta'_{xz}$ and that due to the north–south flow, $D\theta'_y$. This gives

$$D\theta'_{xz} = 1.6\%\ \mathrm{h}^{-1}$$
$$D\theta'_y = -0.9\%\ \mathrm{h}^{-1}$$
$$Dq_{xz} = 2.5\%\ \mathrm{h}^{-1}.$$

Thus the decrease in relative humidity due to the advection of warm air in the north–south direction is about 20% of the increase that occurs in the cross-front direction.

TABLE 2. Fluxes of potential temperature and moisture for run 1 (rates are per day).

At t =	$F(\theta)_{xz}$ (°C)	$F(\theta)_y$ (°C)	$F(q)_{xz}$ (g kg^{-1})	$F(q)_y$ (g kg^{-1})
6 h	−0.9	0.03	1.2	0
37 h	−6.0	+3.5	5.3	0

The same analysis has been performed for run 2, which has a gradient of q specified in the north–south direction. The fluxes of potential temperature and q are summarized in Table 3.

Comparison of Table 3 with Table 2 shows that, as expected, the fluxes of heat and moisture are similar before the first convective line is generated. After the formation of the first line, the potential temperature fluxes show a slight increase of about 20%; however, it is the moisture fluxes that are substantially different. There is now a flux of 1.7 g kg^{-1}/day in the north–south direction, and the cross-front circulation produces an increase of 8.5 g kg^{-1}/day, which is 60% greater than before.

As before, we calculate the changes in relative humidity that these fluxes cause and obtain

$$D\theta'_{xz} = 1.8\%\ \mathrm{h}^{-1} \quad D\theta'_y = -1.0\%\ \mathrm{h}^{-1}$$
$$Dq_{xz} = 3.9\%\ \mathrm{h}^{-1} \quad Dq_y = 0.91\%\ \mathrm{h}^{-1}.$$

As is to be expected $-D\theta'_y \approx Dq_y$ since we have chosen $\partial q_g/\partial y$ so that the relative humidity of the basic state does not vary in the y direction.

e. *Varying moisture profile and frontal circulation*

In the previous sections we have seen that for a particular parameter regime the generation of convection at a surface front is not a continuous process but is periodic. The period of this oscillation in the low resolution, hydrostatic model is of the order of 20–27 hours. In this section we shall vary some of the system parameters to show that the oscillation occurs over a reasonably wide range of values.

The parameters that will be varied are

(i) The moisture profile. For a given cross-front circulation, the relative humidity profile specified at the commencement of the simulation will determine how long it takes before convection is generated.

(ii) The strength of the cross-front circulation. Con-

TABLE 3. Fluxes of potential temperature and moisture for run 2 (rates are per day).

At t=	$F(\theta)_{xz}$ (°C)	$F(\theta)_y$ (°C)	$F(q)_{xz}$ (g kg^{-1})	$F(q)_y$ (g kg^{-1})
6 h	−0.9	~0	1.3	−0.1
37 h	−7.3	4.2	8.5	1.7

versely to (i), for a given relative humidity profile the strength of the ascending motion ahead of the front will determine when convection begins.

It should be noted that in the following simulation we set $\partial q_g/\partial y = 0$.

1) Varying the maximum relative humidity, Rh2. The results of simulations with Rh2 = 0.79 and Rh2 = 0.945 are summarized in Table 4(a), along with the results from run 1. As is to be expected, the first system occurs earlier when Rh2 is increased toward 95% (since less lifting is required to produce condensation). Also, the time period between the two convective systems is decreased as Rh2 increases.

2) The strength of the frontal circulation can be varied by changing the frontal width (varying x_L). The results from run 1 and simulations with x_L reduced by factors of 0.7 and 0.5 are summarized in Table 4(b). Again a periodicity in convection occurs, this time with the period decreasing slightly as the width of the frontal zone is decreased.

The preceding simulations indicate that the periodic generation of convection at a front does not only occur for the particular atmospheric system that we have chosen in run 1, but occurs over a reasonably wide range of parameters. At this juncture it does not seem wise to attempt a detailed explanation of the dependence of the convective period on the parameters varied because of the relatively crude representation of convection in the model.

f. Explaining the periodicity in convective activity

To elucidate the mechanism behind the periodicity in convective activity, we first note that when the second convective system develops, the low-level convergence and vertical velocity are significantly greater than in the steady front. The budget analysis (Table 2) shows that the moisture convergence is 4–5 times greater before the second line develops than before the first develops. In Fig. 6b at t = 40 h, the vertical velocity in the region where the second cloud is developing is 5 cm s^{-1} compared with 0.7 cm s^{-1} in the steady state front.

It is clear that the balanced frontal circulation cannot be used to explain the development of the second convective system. How then does a front that is out of geostrophic balance behave? In section 2a it was shown that if we commence integration with a front that does not contain the initial cross-front circulation an oscillation occurs which has a period of about 12 hours (see Fig. 2). At this juncture it is important to note that although this front is in geostrophic balance at $t = 0$, it is immediately forced out of balance by the differential advection of the along-front gradient of potential temperature.

TABLE 4(a). Time between convective systems for different values of Rh2.

	Rh2	Peak time of first system	Peak time of second system	Time difference
Run 5	0.79	37.2 h	69.4	32.2
Run 1	0.84	27.8 h	54.8	27.0
Run 6	0.945	17.5 h	40.6	23.1

TABLE 4(b). Time between convective systems for different values of x_L.

	x_L (km)	Peak time of first system (h)	Peak time of second system (h)	Time difference (h)
Run 1	158	27.8	54.8	27.0
Run 7	112	27.2	53.7	26.5
Run 8	79	25.5	51.3	25.8

The oscillation in the dry front circulation is essentially caused by the propagation of inertial gravity waves away from the frontal region. The horizontal and vertical scale of these inertial gravity waves is set by the scale of the frontal circulation, which in turn is set by the scale of the frontal forcing. We can thus gain an estimate of the horizontal and vertical wavelengths of the inertial gravity waves generated by the frontal forcing by doubling the horizontal and vertical halfwidths of the circulation, respectively. For the circulation shown in Fig. 1 we obtain a horizontal wavelength of λ_H = 680 km and vertical wavelength λ_v = 7200 m. The period of an inertial gravity wave in an environment with no mean flow is

$$T = 2\pi/(f^2 + N^2\lambda_v^2/\lambda_H^2)^{1/2}. \quad (12)$$

(We justify using the equation for no mean flow by the fact that the horizontal velocities in the region of the front, ~2–3 m s^{-1}, are small in comparison with the horizontal inertial-gravity wave speeds ~20 m s^{-1}.) The stability parameter N^2 is difficult to estimate, as it varies substantially across the front. However, an estimate of N^2 can be obtained by averaging the stratification in both the horizontal and the vertical in the region of the frontal circulation. Averaging in this manner gives $N^2 = 1.1 \times 10^{-4}$ s^{-2}. With $f = 10^{-4}$ s^{-1} we obtain an inertial-gravity wave period of T = 11.8 h, which agrees well with the period of 12 hours for the frontal oscillation.

The circulation in the moist convective frontal system is considerably more complex than the dry frontal circulation; nevertheless, it is similar in respect to the fact that the front is forced out of geostrophic balance (in this case by the first convective system). This system produces subsidence in the frontal zone which "flattens" the isentropes and v contours (see the schematic diagrams in Fig. 10). The term $f\partial v/\partial z$ becomes large and positive, whereas $\partial\theta/\partial x$ tends to zero, giving a positive ageostrophic residue

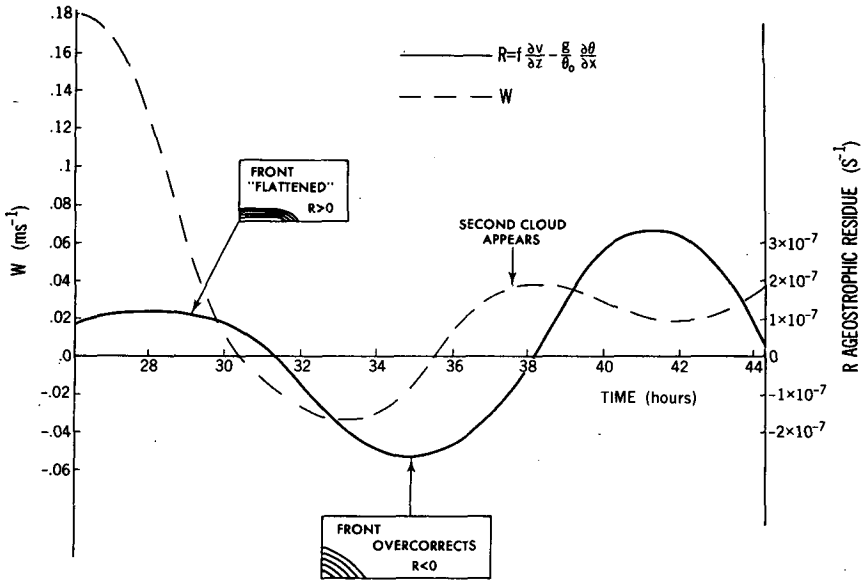

FIG. 10. Vertical velocity from run 1 in the region where convective systems develop (dashed line). Also the ageostrophic residue averaged in the region of the front (solid line).

$$R = f\frac{\partial v}{\partial z} - \frac{g}{\theta_0}\frac{\partial \theta}{\partial x}.$$

In Fig. 10 the mean ageostrophic residue in the front is plotted (for the purposes of the present analysis the front is defined as the region where $\theta' < -2.0°C$). As can be seen for the period up to 31 h, $R > 0$, indicating that the isentropes are "flatter" than that required for geostrophic balance. We can estimate the importance of this ageostrophic residue by comparing the individual terms in the full equation for the cross-front circulation

$$N^2\frac{\partial^2\psi'}{\partial x^2} + f\left(f + \frac{\partial v}{\partial x}\right)\frac{\partial^2\psi'}{\partial z^2} - \left(2f\frac{\partial v}{\partial z} - R\right)\frac{\partial^2\psi'}{\partial x \partial z} = -2f\frac{\partial v}{\partial x}\frac{\partial U_g}{\partial z} - \frac{DR}{Dt}. \quad (13)$$

Equation 13 shows that the cross-front circulation is forced not only by the shearing term

$$-2f\frac{\partial v}{\partial x}\frac{\partial U_g}{\partial z},$$

but also by the rate of change of R following the motion, DR/Dt. Again we can approximate DR/Dt by $\partial R/\partial t$, as the advective velocities in the front are small. From Fig. 10 the maximum rate of change of the mean value of R in the front is

$$\partial R/\partial t \approx 0.22 \times 10^{-11}\,\mathrm{s}^{-3}.$$

The average value of the shearing term

$$-2f\frac{\partial v}{\partial x}\frac{\partial U_g}{\partial z}$$

in the front is $0.16 \times 10^{-11}\,\mathrm{s}^{-3}$. These estimates indicate that the unsteady ageostrophic forcing term exceeds the steady shearing term and hence can cause a reversal of the cross-front circulation.

However, the first system not only causes an imbalance in the surface front, but also in the rest of the environment surrounding the convective system. In these regions an ageostrophic residue is created as soon as potential temperature gradients develop (since $\partial v/\partial z$ is initially zero).

As the first system decays, the atmosphere attempts to return to geostrophic balance. As previously discussed, for the case of a dry front, this is achieved by the propagation of inertial gravity waves away from the region of imbalance. The effect of these inertial gravity waves in the frontal zone is clearly shown in Fig. 10. The ageostrophic residue changes sign as the front is pushed back (see Fig. 4 also) and the isentropes become highly sloped. Also plotted in Fig. 10 is the vertical velocity in the region where the second system develops and as can be seen during this time (t = 31–35 h), there is descent in the frontal zone. Half a period later the front surges forward, the air ahead of the front ascends and the second cloud appears (at about t = 37.5 h).

g. The time period of the oscillation

Figure 10 clearly shows that the oscillation in vertical velocity and ageostrophic residue has a period of approximately 12 hours. What actually determines this period is a complex problem and one that is beyond the scope of the present work. Clearly, the dominant inertial gravity waves that are formed will have a period

which is of the same order as the lifetime of the convective system. (In section 3b it will be shown that the lifetime of the convection is essentially limited by the drying out of the system's inflow.) It is interesting to note that the 12-h period is similar to the period found in section 2a for a dry front that is forced out of geostrophic balance; however, it is not known at present whether this is merely coincidence. Clearly this is an area that requires further work; at present we can only state that the second convective system is generated by the increased convergence that occurs as the front and environment return to geostrophic balance.

The author's attention has recently been drawn to a related work by Ogura and Jiang (1985). They used a two-dimensional cloud model to examine a mesoscale convective system that occurred on 10–11 April 1979 during the AVE-SESAME observational experiment. Included in their model is a horizontally uniform but vertically varying large-scale forcing (taken from observations) that is applied for the duration of the experiment. Convection is generated by this large-scale forcing (as it is in the present work); however, as the forcing has no horizontal variation there is no localization of convection as there is in the present simulations.

Ogura and Jiang (1985) also find a periodicity in convective activity (see their Figs. 12 and 16) with the second system developing some 5 hours after the decay of initial convective activity. (The results with the nonhydrostatic model, to be discussed later, indicate a time period of approximately 7 hours between decay of the first system and generation of the second, see Fig. 12.) They hypothesize that the first system decays because it dries out the subcloud layer, and the next system develops when the large-scale lifting has moistened these layers. In the present work we find a similar behavior; however, it is also found that the large-scale convergence and lifting (which is specified constant in time in the work of Ogura and Jiang, 1985) is substantially modified by the first system. In fact, as shown by Table 2, the large-scale convergence is almost an order of magnitude greater before the development of the second system compared to that before the development of the first system.

In the work of Ogura and Jiang (1985) no increase in low-level convergence is possible, as 1) the large-scale forcing is specified to be constant in time and 2) periodic boundary conditions are applied so that there can be no convergence (other than that specified) into the model domain at low levels.

To summarize: both in the present work and the work of Ogura and Jiang (1985), a periodicity in convective activity is found. The periodicity appears to occur when the first system dries out the subcloud layer and decays. The second system is then generated when low-level convergence destabilizes the atmosphere again. In the present work it is found that the low-level convergence before the generation of the second system is substantially enhanced by the action of the first system, whereas in the work of Ogura and Jiang (1985) the convergence is specified constant with time.

Before concluding this section it should be noted that with the hydrostatic model, the second system does not reach its maximum intensity until some 16 hours after convergence returns to the frontal zone (see Fig. 4). In other words, the period in convective activity is significantly longer than the period of the oscillation in low-level convergence. This is primarily due to the fact that convection is simulated only crudely in the hydrostatic, low-resolution model and tends to develop much more slowly than in reality. In the next section a nonhydrostatic model with higher resolution will be used to study the same system, and it will be seen that the period of the oscillation in convective activity is significantly reduced.

3. Simulations with a nonhydrostatic model

a. Description of model

The nonhydrostatic model to be used is a two-dimensional version of the anelastic three-dimensional cloud model described in Lipps and Hemler (1982). The subgrid-scale mixing terms have been modified from Lipps and Hemler (1982) to allow for the effects of reduced mixing in regions of higher stability and for anisotropy in the grid spacing.

The horizontal resolution, $\Delta x = 2.8$ km, is five times that used in the hydrostatic model. The vertical grid-length is 500 m, and the top of the model is placed at 13.8 km. Test simulations indicated that a reasonably strong damping layer (with an average damping time of 4 minutes specified above 10 km) was required to reduce reflections of the upper boundary. Although this damping most likely has a significant effect on convection in the upper troposphere, the influence on the motion of interest in this paper, the low-level convergence initiating convection, is probably minimal.

Rain is also included as a prognostic variable in the model, as outlined in Lipps and Hemler (1982). This makes it possible to study the effects of evaporative cooling and the formation of gust fronts which are an important feature of squall line dynamics. Simulations with explicit rain (run 9) and with the simplified rain-parameterization scheme used in the hydrostatic model (run 10) were performed to study the importance of evaporative cooling.

The initial fields, including the cross-front circulation discussed in section 2a, are the same as that specified for the hydrostatic model. Again, the relative humidity is 55% at the ground and 5% at the top of the domain. In order to obtain early development of convection (and thus a saving in computer time) the maximum relative humidity, Rh2, (which occurs at $z = 2250$) is set to 99.5%.

To further save computer time, the width of the domain was decreased by 24% (giving 458 gridpoints in

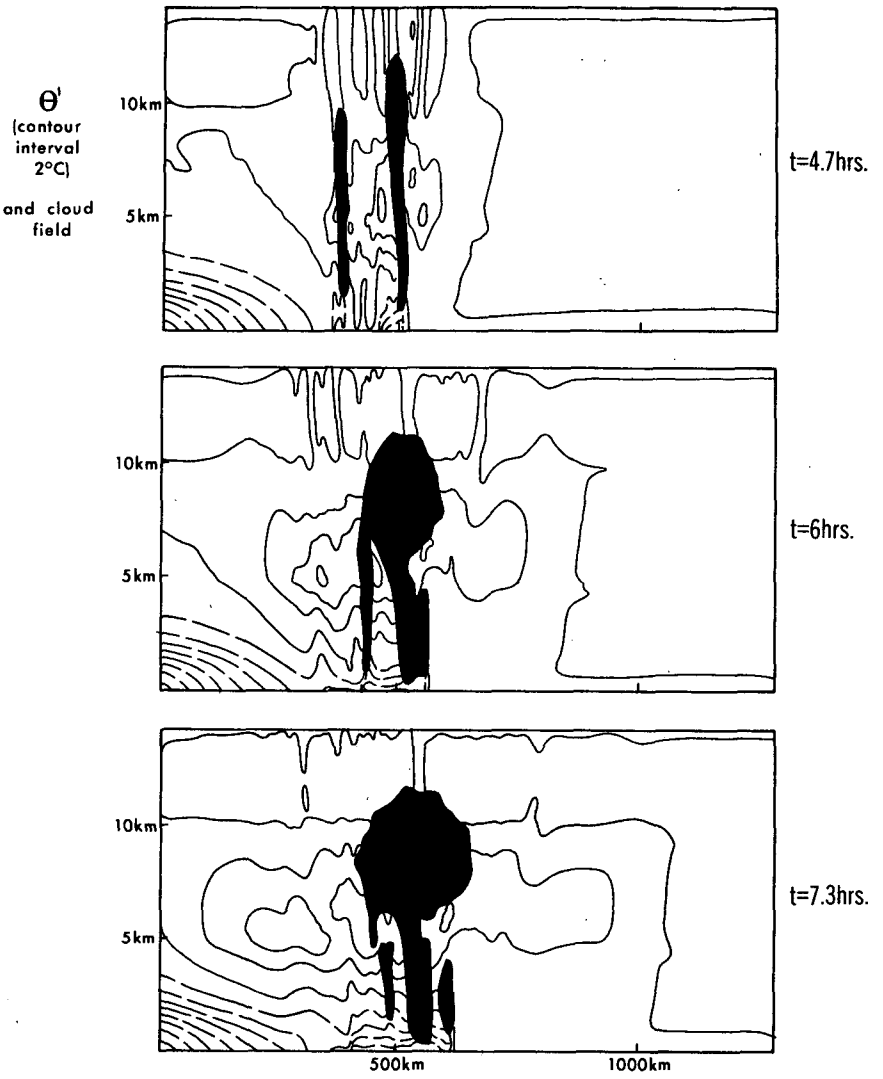

FIG. 11a. θ' and cloud fields for run 9 (with the nonhydrostatic model). Note the dome of cold air, formed by evaporative cooling, below the convective system.

1270 km). In the simulations to be described the first convective line often approaches the left-hand boundary before the development of the second convective system. Although the boundary conditions at this time obviously have an important effect on the first convective system, it is again felt that the effect on the low-level convergence generating the second system is minimal.

b. Results

As in the hydrostatic model, cloud first appears in the ascending branch of the circulation ahead of the surface cold front. Due to the increased resolution there are now some 60 or so gridpoints in this initial cloud region. This means that several circulations in this region can be resolved, as distinct from the one cell that develops in the hydrostatic model. At $t = 4$ hours (not shown) there are three distinct cells. Forty minutes later the center cell has been suppressed, leaving two cells approximately 100 km apart (Fig. 11a). As can be seen, the right-hand cell grows faster than the left-hand cell. Furthermore, the low-level flow into the stronger cell tends to "attract" the weaker cell towards it. The two updrafts approach at about 6 m s^{-1}, with the clouds merging aloft at 6 h and the lower sections merging at $t = 9$ h. (The ψ field at $t = 9.3$ h is shown in Fig. 16. This figure is used in section 3c to compare with the results from the hydrostatic model).

The mechanism by which a strong cell attracts weaker cells toward it was studied by Orville et al. (1980). In their study, the separation between the individual clouds was less than 10 km. They found that if one cell was generated some time earlier than the

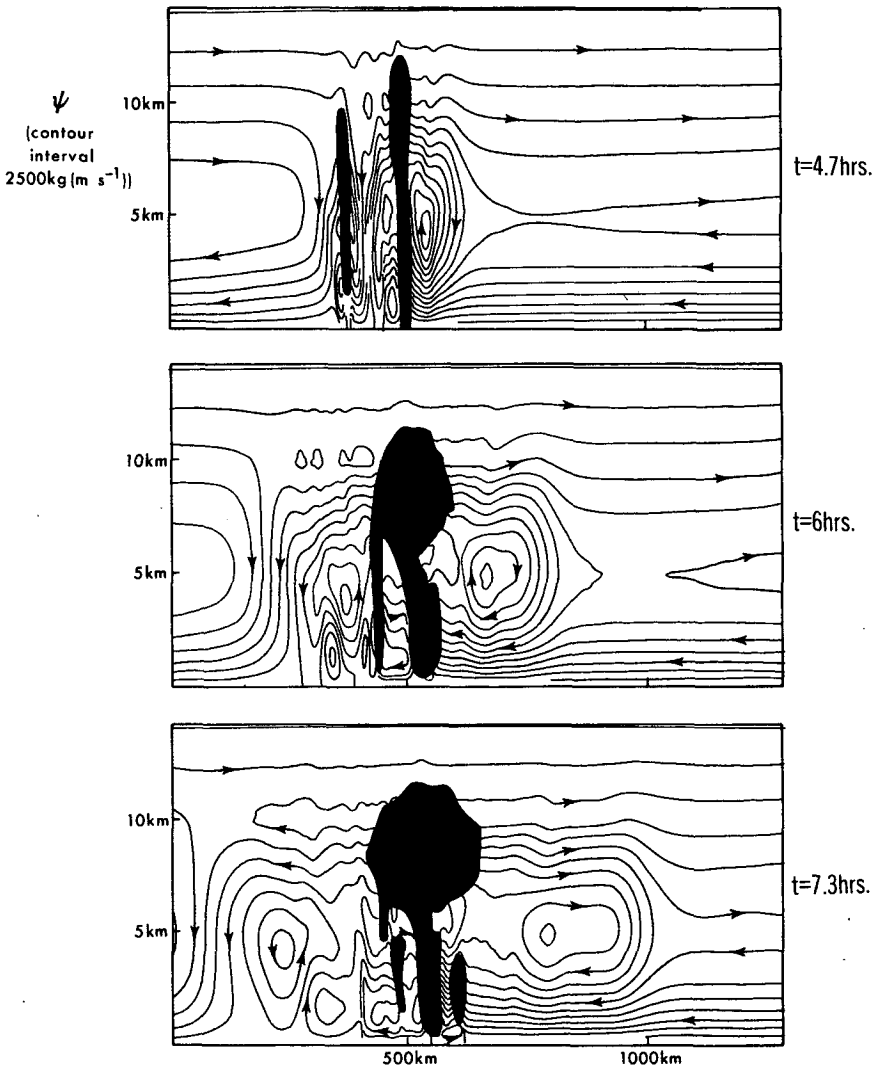

FIG. 11b. Streamfunction in a frame of reference in which the convective system is at rest.

second (6 minutes being the optimum time difference found in their study), the clouds merged after about 30 minutes (see their Fig. 4). In the present study we have found a similar behavior, except on a horizontal scale which is an order of magnitude greater.

The maximum vertical velocity for this simulation is plotted in Fig. 12. As can be seen, the first system lasts for approximately 11 hours. The second system (which is shown in Fig. 13) then begins growing some 7 hours later; this supports the hypothesis developed in section 2f that the second system is initiated when the dominant inertial gravity mode produces convergence again in the frontal zone.

It is important to note, however, that the time period between the initiation of the first and second systems is about 20 hours, which is greater than the inertial gravity period. This occurs because the first system persists for longer than half a period. The mechanisms that control the system's lifetime are discussed briefly in the next section.

1) LIFE OF THE CONVECTIVE SYSTEM

As noted in section 2f and discussed in Ogura and Jiang (1985), the convective systems decay essentially because they dry out the subcloud layer. The subsidence that occurs in the environment surrounding the convective system decreases the relative humidity of the environment and, most importantly, that of the inflow to the convection. Thus, once the convection has commenced, the air in the inflow, which has been subjected to the compensating subsidence, needs to be lifted through a greater distance before condensation will occur.

The drying out of the environment is clearly shown in Fig. 14. This shows the relative humidity field at *t*

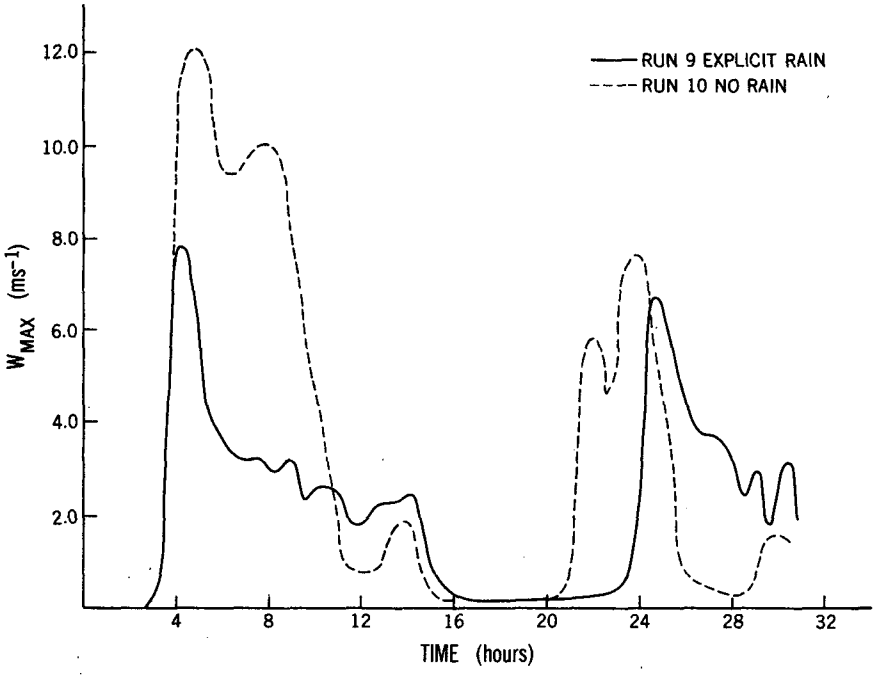

FIG. 12. Maximum vertical velocity for runs 9 and 10.

= 6.7 hours. The initial relative humidity field can be seen at the right-hand boundary (where the compensating subsidence has not yet reached). As can be seen, the relative humidity around the convective system has been substantially reduced. In the inflow region, where the maximum relative humidity was initially 99.5%, the maximum has been decreased below 88% in most regions. At the level of the inflow a 1% decrease in relative humidity is approximately equivalent to a subsidence of 25 m; thus, the air at these levels has been forced down by at least 300 m. Before this air can convect it has to be lifted through this extra distance; after a certain time the latent heating in the convective system is not sufficiently strong enough to cause this extra lifting.

2) RUN 10: SIMULATION WITH NO EVAPORATIVE COOLING

The nonhydrostatic model was also run with the rain parameterization scheme used in the hydrostatic model: i.e., removal of any cloud water greater than a concentration of 1.5 g kg^{-1}. The maximum vertical velocity in the domain is plotted in Fig. 12; as can be seen, the vertical velocities are more intense. However, the lifetime of the first system is slightly less than in the simulation with explicit rain. In section 3c it is shown that the mass flux of the first system in the two simulations is approximately the same.

The similarity between runs 9 and 10 suggests that rain does not play a major role in the long-term behavior of the squall line and cold front, although it does modify the structure of the whole system. Some of these modifications can be seen in the θ' field (Fig. 11a). Evaporation of rain produces a dome of cold air below the convection, and this spreads both towards the cold front and away from it. At the forward edge of the cold pool (i.e., the boundary moving away from the front) new convection can be seen forming. The other boundary of the cold dome eventually meets with the cold air in the front. At this time it becomes difficult to determine if the cold air at the ground is part of the original cold front or is due to evaporative cooling. Connected with this is the question of what represents the leading edge of the front. This problem has arisen in many observational studies of cold fronts. Here we will not attempt a detailed analysis of this problem; however, two comments can be made from the present numerical results. First, the second squall line forms at the forward edge of the rain-cooled air and not at the point where this cold dome meets the original cold front. The forward edge of the cold dome is also the position of the low-level poleward jet discussed in section 2b. Figure 15 is a plot of the v field and cloud field at t = 23.3 h (just as the second system is commencing) and this shows that the second system develops very close to the center of the poleward flow.

The second and somewhat surprising observation on the problem of evaporative cooling in the frontal region is that the position of the forward edge of the cold dome in run 9 is very close to the leading edge of the cold front in run 10 without evaporative cooling. In other words, the position of the low-level jet and the position of development of the second convective

system is approximately the same in the two simulations. This suggests that evaporative cooling and the formation of forced downdrafts are not crucially important to the overall dynamics of the front, especially the propagation speed of the front.

c. *Comparison between hydrostatic and nonhydrostatic simulations*

In this section we will compare run 9 (nonhydrostatic, Rh2 = 0.995) with run 6 (hydrostatic, Rh2 = 0.945). (As already stated there is little difference between run 6 and a hydrostatic simulation, with Rh2 = 0.995 and the saturation criterion set at 100%.) Both run 6 and run 9 commence with a maximum relative humidity which is 0.5% below the saturation criterion. Thus saturation first occurs at the same time in the two simulations. However, convection occurs much later in the hydrostatic low-resolution model, which is primarily because the smaller-scale convective motions which have faster growth rates cannot be resolved in that model.

In Fig. 16 the streamfunction and cloud fields from the nonhydrostatic simulation are shown at $t = 9.3$ h, which is approximately the midtime of convective activity. The hydrostatic fields are also shown at the midtime of convection; however, because of the slower onset of convection in the model, this time is about 8 hours after that in the nonhydrostatic model (see Fig. 17).

The maximum vertical velocity in run 6 is 1.64 m s^{-1}, which compares with about 7.5 m s^{-1} in the nonhydrostatic simulation. A large proportion of this difference is associated with the higher resolution in the nonhydrostatic model. In Fig. 17a the maximum vertical velocity is plotted again for the two simulations, except this time a five-point average is applied to the nonhydrostatic fields to give the same effective resolution as the hydrostatic model. The hydrostatic results are also shifted forward by a period of 8 h to bring the evolution of the two systems into line. As can be seen from Fig. 17a, averaging the fields in the nonhydrostatic model to the same resolution as the hydrostatic model reduces the maximum vertical velocity by a factor of almost 2; nevertheless, the velocities remain about two times greater than in the hydrostatic model.

The two models are quite similar, however, if the vertical mass flux in the cloud is used as a measure of the strength of convection rather than the maximum vertical velocity. The mass flux in the cloud (at the level of maximum vertical velocity) is plotted in Fig. 17b. The behavior with time is somewhat different between the two models; however, the total mass fluxes are within 12% of each other, with the hydrostatic model giving a greater mass flux.

It is interesting to note that this result occurs despite the fact that the nonhydrostatic model has explicit precipitation, whereas in the hydrostatic model rain is only represented by removing any cloud above a concentration of 1.5 g kg^{-1}. To further illustrate the lack of sensitivity to the exact nature of the precipitation scheme, the mass flux for run 10 (nonhydrostatic but with the hydrostatic "rain" scheme) is also plotted in Fig. 17b. Again the behavior of the mass fluxes are quite similar, with run 9 having 12% greater total mass flux than run 10.

Because of the large difference between the nature of the two models, it does not seem wise to further compare the two sets of results. However, it is encouraging that the two models give similar lifetimes for the convection and similar convective mass fluxes (as these determine the strength of the frontal forcing) while the actual onset of convection is delayed in the low-resolution model.

4. Observations of periodicity in convective activity

In the previous sections it has been shown that a numerically modeled surface front exhibits a periodicity in convective activity at the leading edge of the front and that this is most likely caused by an inertial gravity oscillation in the low-level convergence. To uncover this periodicity in the real atmosphere we first need to consider the additional complexities of the atmosphere that are not modeled in the numerical system. Four of these additional complexities are listed as follows.

(i) Three-dimensionality of squall lines in the real atmosphere can only be crudely considered as two-dimensional convective systems as they usually consist of a series of cells that move along the line. However, at some distance from the line of cells (for example, in the region of the front) the forcing provided by the cells should appear, to a reasonable approximation, to be two-dimensional. Nevertheless, the squall line usually forms only in a certain region of the front; hence, an ageostrophic residue will only be produced in that region. The inertial gravity waves which are generated by the squall line will then propagate relative to the mean wind and this wind generally has a component along the front toward the north. Thus, the region where convergence returns to the front will be further along the line to the north of the region where the first squall line formed. This movement of the region of low-level convergence along the line of the front is evident in the observations to be presented at the end of this section.

(ii) The second complicating feature of the real atmosphere is the variation of temperature and humidity profiles that the front can experience. For example, a front that is moving at 10 m s^{-1} travels almost 450 km in 12 hours (which is approximately the period of inertial gravity waves found in the model), and the temperature and humidity fields can vary considerably over that distance. Thus, even though convergence may return to the frontal region after the decay of the first

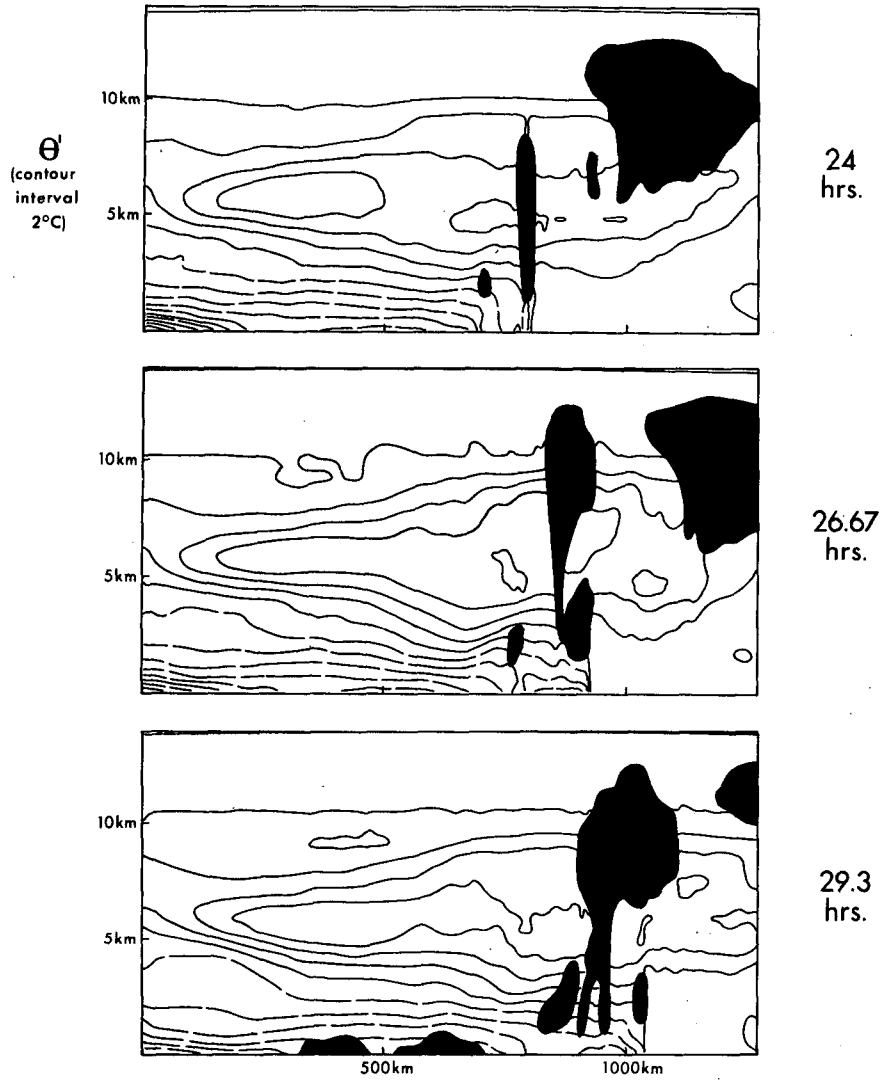

FIG. 13. The development of the second convective system in run 9. (a) θ' field.

squall line, there may not be further development of convection if the front moves in to a region of the atmosphere which is less conditionally unstable.

(iii) The third important feature of the real atmosphere that is not included in the model is surface heating. The diurnal cycle of surface heating makes the atmosphere most unstable in the late afternoon and this is when prefrontal squall lines are most commonly observed (for example, see Palmen and Newton, 1969, p393). Thus, if an oscillation in the low-level convergence occurs with the 12-h period that is common in the numerical model, the convective system which is in phase with the surface heating will be enhanced relative to the system occurring 12 hours later. This bias towards the late afternoon convective system is also evident in the observations to be presented.

(iv) The properties of a real front may change considerably over a period of 24 hours. In the present model where the frontogenetical forcing is weak, the dry surface front is only slightly modified over the duration of the simulation. However, in the real atmosphere, cold fronts are often subjected to strong frontogenetical or frontolytical forcing which can modify considerably the structure of the front over a period of 24 hours. It seems reasonable to hypothesize that for a developing front the second system will be enhanced compared to a steady state front. Conversely, for a front that is decaying the second system will be diminished (or may not develop at all). One of the examples to be studied shows a definite strengthening of the front with time (see Fig. 19).

We first reexamine a case that has been studied extensively, that of 25–26 April 1979, which was part of

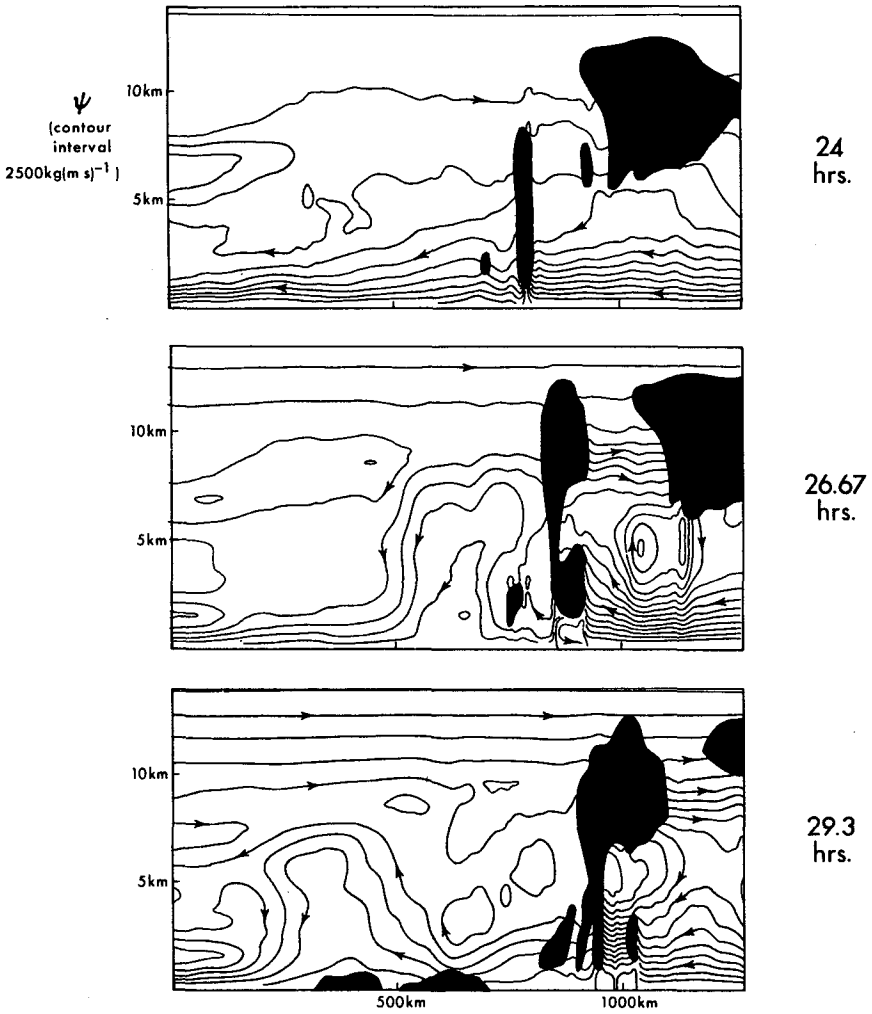

FIG. 13. (*Continued*) (b) Streamfunction in a frame of reference in which the *second system* is at *rest*.

SESAME-AVE III. The squall line that passed through central Missouri late on 25 April and for the first few hours of 26 April has been modeled by Anthes et al. (1982), and Orlanski et al. (1985), while an observational analysis has been performed by Ogura and Portis (1982). There does not appear to be any evidence that strong convection occurred after this event (at least not for the next 12 hours or so); however, approximately 12 hours before this squall line there is good evidence of strong convection occurring ahead of the front. The radar summary charts are shown at 1135, 1635 and 2335 UTC 25 April 1979 in Fig. 18. At 1135 UTC there is clearly a line of convection along the Kansas–Missouri border, with a line further south crossing the Oklahoma–Texas border. This line of convection is also indicated on the surface analysis at 1200 UTC. Five hours later, the radar summary chart shows that convection had largely died out in the area; then seven hours later severe convection broke out along the front (note, however, that the second line has rotated through some 30 degrees relative to the first, a feature which obviously cannot be captured by the two-dimensional

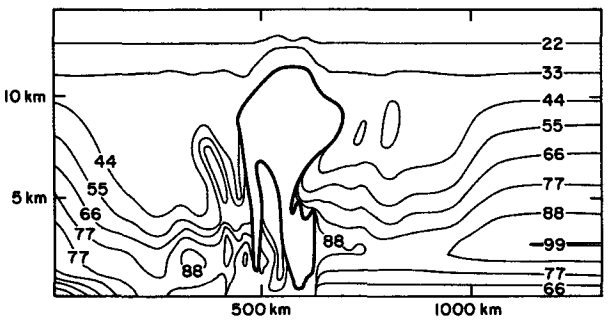

FIG. 14. Relative humidity field for run 9 at $t = 6.7$ h. The outline of the cloud (where the relative humidity equals 100%) is indicated by the thick solid line.

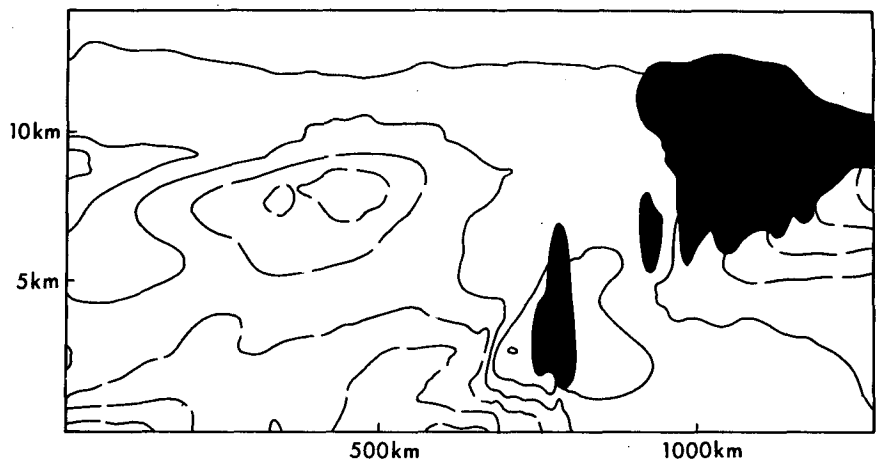

FIG. 15. North–south velocity field and cloud field for run 9 at $t = 23.3$ h. Note that the second convective system forms very close to the poleward jet, i.e., where the environment is destabilized by the advection of warm air (contour interval 5 m s^{-1}).

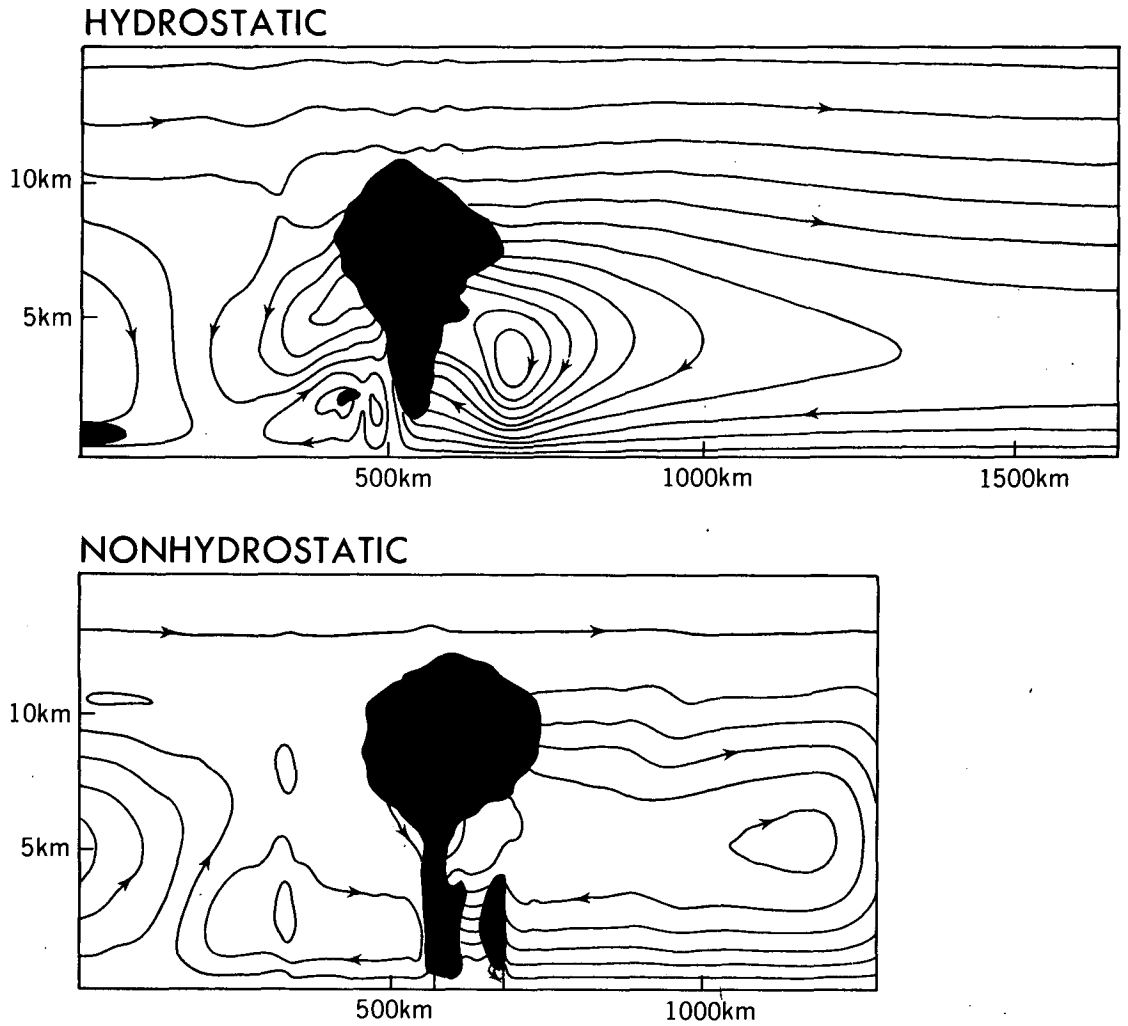

FIG. 16. ψ and cloud fields for runs 6 and 9 [contour interval 4000 kg (ms)$^{-1}$].

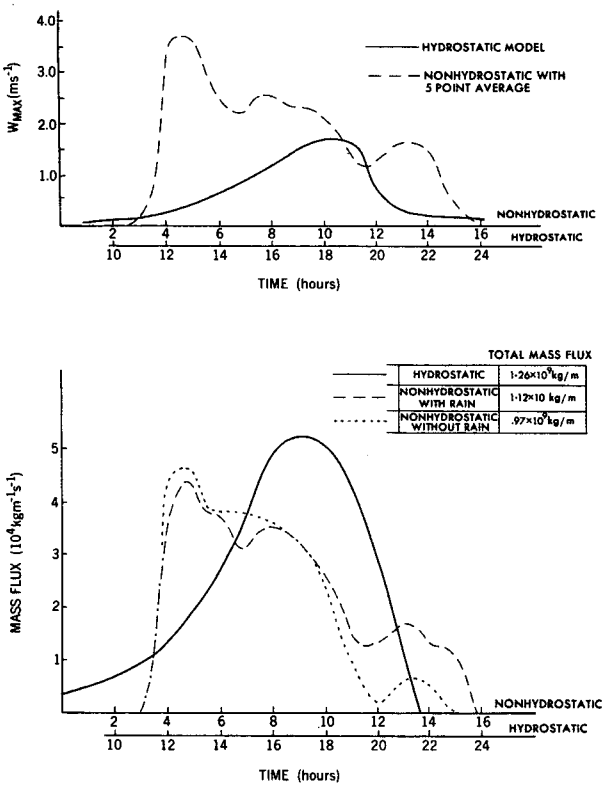

FIG. 17. (a) Maximum vertical velocity for the first system in the hydrostatic model (solid line) and the maximum vertical velocity in the nonhydrostatic model after a 5-point average in the horizontal has been applied (dashed line). (b) Vertical mass flux in the convective system against time for runs 6, 9 and 10.

model). Further evidence of the periodicity in convective activity is given in Fig. 13 of Ogura and Portis (1982), which is a time history of the potential temperature and relative humidity at Monett (marked by a *X* in Fig. 18 at 1135 UTC). The remnants of the first convective system can be seen passing through Monett between 1400 and 1800 by the values of high humidity at 600 mb. Approximately half a day later, the major convective system and cold front moved through the station. The similarity between this figure and the numerical model results (for example, Figs. 6a and 13a) suggest that time histories of relative humidity may give the best indication of the oscillation in convective activity.

Thus, there is some evidence of a periodicity in convection at the front that propagated through the SESAME network on 25–26 April 1979. However, because the second line is rotated relative to the first and also because convection does not appear to break out after the severe line, the evidence is in no way conclusive. In order to find more conclusive evidence of this oscillation, a search was performed of the radar summary charts for the month of April (generally a month in which prefrontal squall lines are common) for the years

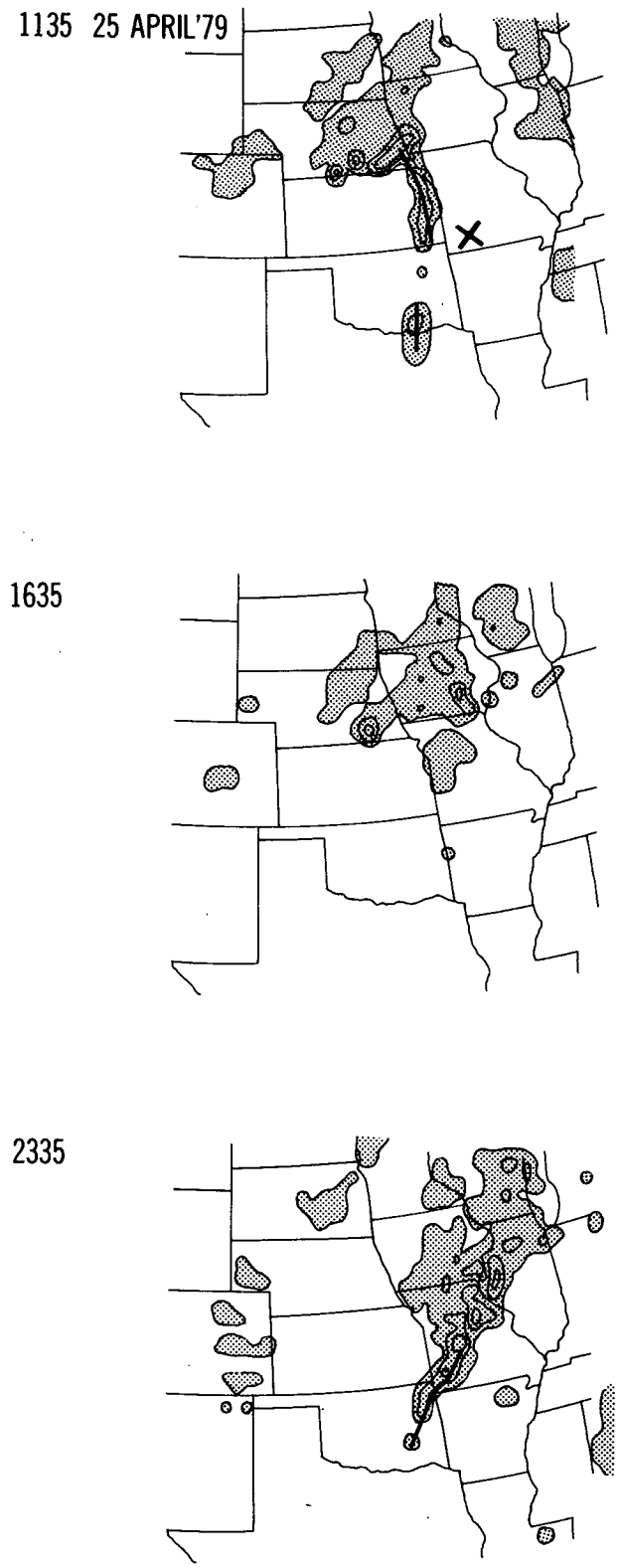

FIG. 18. Radar summary charts for 25 April 1979 showing the squall line that was studied as part of SESAME-AVE 111. The upper-air station at Monett that is used in Fig. 13 of Ogura and Portis (1979) is marked by a *X* on the chart at 1135 UTC.

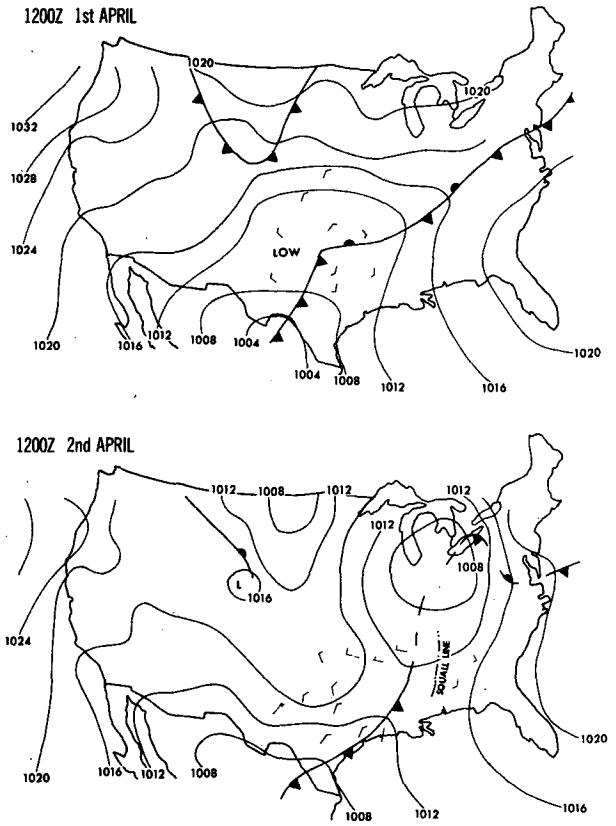

FIG. 19. Surface analysis at 1200 UTC 1 April and 1200 UTC 2 April showing a cold front moving through Texas and Louisiana. Only the surface wind barbs in the region of the front are drawn.

1979–82. Only examples in which three peaks of convective activity are evident are considered, a further criterion is that the convective line be long (of the order of 700 km) compared to its width.

A good example of periodic convective activity occurred on 1 and 2 April and is shown by the radar summary charts in Fig. 20 and the surface maps in Fig. 19. The radar summary charts are shown every 6 hours and it is clear that convection is strong at 0835 UTC 1 April, 2035 UTC 1 April, 0835 UTC 2 April, and weak at times in between. In order to quantify this observation, a domain is defined in the region of the cold front (as shown) and is moved perpendicular to the front at a constant velocity (which is the same as the mean velocity of the front, as analyzed on the surface weather maps, during the period of interest). As a measure of the strength of convection we take the area enclosed by the second contour (the "3" contour, which corresponds to a certain value of dBZ) and plot this as a percentage of the total area of the domain. The results of this analysis are shown in Fig. 21 (the percentages have been time smoothed with a 1-2-1 filter each hour). An oscillation is clearly evident and has a period of approximately 13 hours. Note also that the central peak which occurs in the late afternoon is greater than the two other peaks.

There is a clear tendency, evident in Fig. 20, for the region of maximum activity to move along the line toward the north. As already discussed, the region where low-level convergence returns to the frontal region will move with the mean low-level wind, which is primarily along the front towards the north.

Two further examples (4 April 1981 and 17 April 1982) are plotted in Fig. 22. In the first, the dominant oscillation has a period of 11 h, with the late afternoon convective system being significantly more intense than the convection before and after. In the 17 April 1982 case the situation is more complex, as a shorter timescale oscillation is apparent over the first 16 hours or so of analysis. The shorter oscillation has a period of about 6 hours and there is some evidence of this oscillation in the other case studies.

Finally, a preliminary investigation of the Oklahoma squall line of 10–11 June 1985 (which occurred during the PRESTORM observational experiment) indicates that the convective activity was periodic in nature. Radar summary charts show an intense convective line crossing the Texas panhandle and northwest Oklahoma at 0135 UTC. The convective line decayed 4 to 6 hours later, and then a further intense line (with peaks to 16 km) appeared at 0935 UTC in southeastern Oklahoma. Observations of this event are presently being studied in more detail.

In conclusion, it is felt that there is some observational evidence for an oscillation in convection at a surface front and that this oscillation often has a period of about 12 hours. The evidence, however, is in no way conclusive and clearly further work needs to be done in this area. Nevertheless, the observations have been useful in indicating the additional complicating features of the real atmosphere that are not modeled in the numerical system.

5. Conclusions

In the present study we have attempted to elucidate some of the features of the circulation at a cold front in the presence of moist instability. The features discussed are

(i) The generation of a large convective system (with a horizontal length scale of 200 km) in the ascending branch of the circulation ahead of the front.

(ii) The formation of a low-level poleward jet ahead of the front by Coriolis turning of the flow into the convective system.

(iii) The generation of further convection after the first line has decayed. In the hydrostatic model the time between the generation of the two systems is on the order of 20–27 hours, whereas in the nonhydrostatic model the time period is 18–20 hours. The difference between the results of the two models is explained by the low resolution of the hydrostatic model.

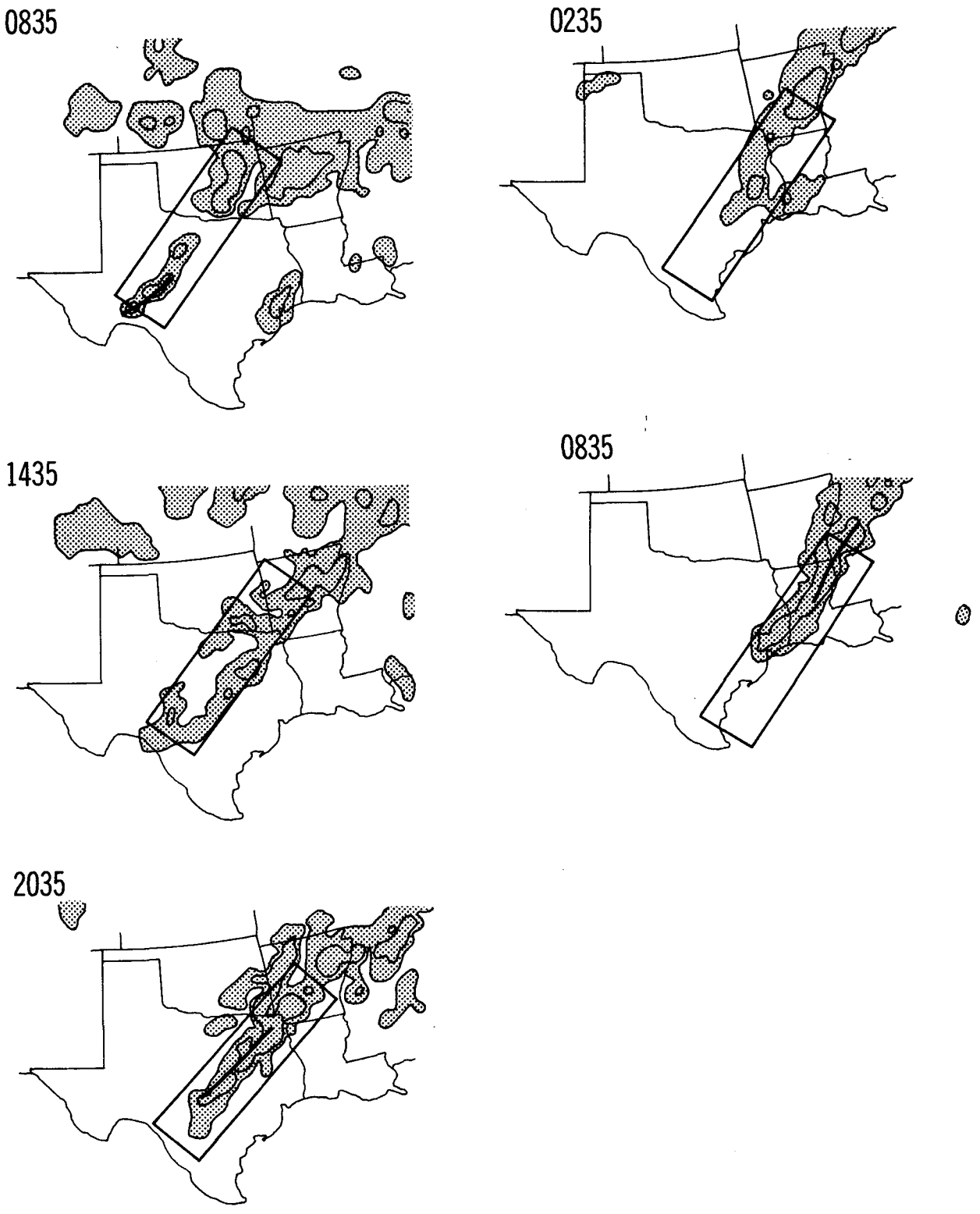

FIG. 20. Radar summary charts at six hourly intervals in the region of cold front shown in Fig. 18. Only the "1" and "3" contours from the summary charts are drawn. As in Fig. 17, the thick solid line indicates a continuous line echo on the radar screen. The rectangular analysis domain is moved perpendicular to the front and at the same speed as the front.

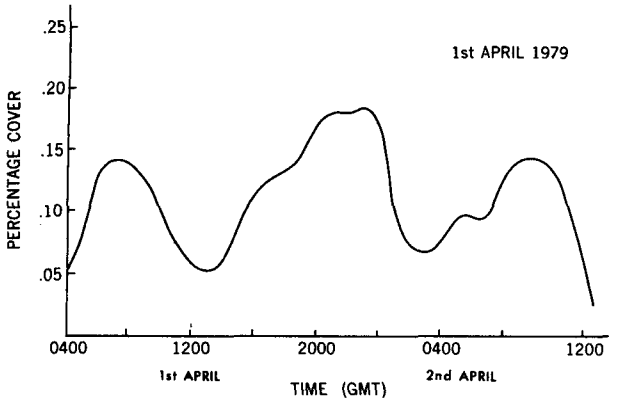

FIG. 21. The area (expressed as a percentage of the total area of the analysis domain) enclosed by the "3" contour on the radar summary charts.

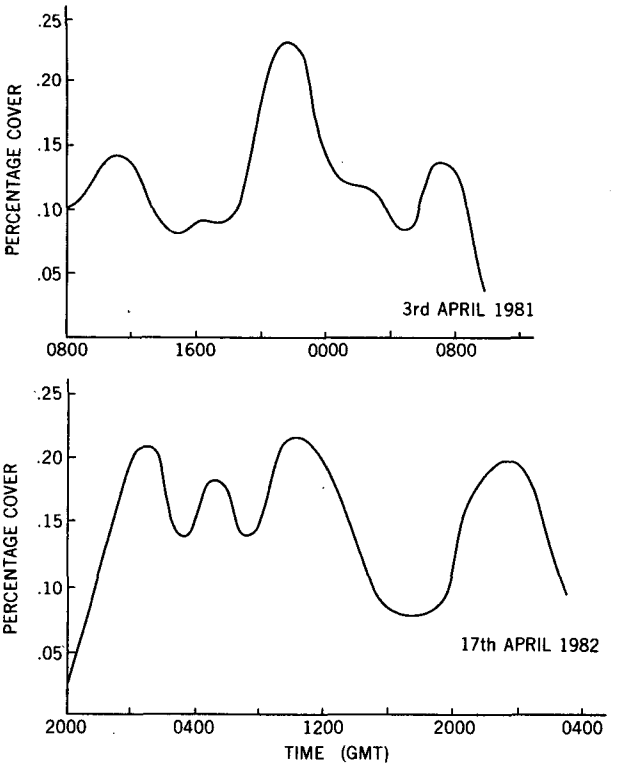

FIG. 22. Similar analysis as in Fig. 20, except for fronts on the 3 April 1981 and 17 April 1982.

The periodicity in convective activity is explained in the following terms. The first convective system decays when its compensating subsidence dries out the flow into the convection. The second system then develops when low-level convergence destabilizes the atmosphere again. It has been shown that the first system forces an oscillation (with a period of the order of 12 h) in the low-level convergence such that upward motion returns to the frontal zone half a period (6–7 h) after the decay of the first system.

Acknowledgments. The author would like to thank the following for helpful discussions on the present work: I. Orlanski, F. Lipps, B. Ross, R. Hemler, R. Rotunno and M. Moncrieff. An anonymous reviewer who brought the work of Ogura and Jiang (1985) to the author's attention is gratefully acknowledged. The figures were drafted by P. G. Tunison and staff. The financial support given by the Geophysical Fluid Dynamics Program at Princeton University under NOAA Grant NA84-EAD00057 is gratefully acknowledged.

REFERENCES

Anthes, R. A., Y. Kuo, S. G. Benjamin and Y. F. Li, 1982: The evolution of the mesoscale environment of severe local storms: Preliminary model results. *Mon. Wea. Rev.*, **110,** 1187–1213.

Browning, K. A., and T. W. Harold, 1970: Air motion and precipitation growth at a cold front. *Quart. J. Roy. Meteor. Soc.*, **96,** 369–389.

Crook, N. A., 1986: The effect of ambient stratification and moisture on the motion of atmospheric undular bores. *J. Atmos. Sci.*, **43,** 171–181.

Hoskins, B. J., 1982: The mathematical theory of frontogenesis. *Ann. Rev. Fluid Mech.*, **14,** 131–151.

Hsie, E., R. Anthes and D. Keyser, 1984: Numerical simulation of frontogenesis in a moist atmosphere. *J. Atmos. Sci.*, **41,** 2581–2594.

Keyser, D., and R. A. Anthes, 1982: The influence of planetary boundary layer physics on frontal structure in the Hoskins-Bretherton horizontal shear model. *J. Atmos. Sci.*, **39,** 1783–1802.

——, and ——, 1986: Comments on "Frontogenesis in a moist semigeostrophic model." *J. Atmos. Sci.*, **43,** 1051–1054.

Lipps, F. B., and R. S. Hemler, 1982: A scale analysis of deep moist convection and some related numerical calculations. *J. Atmos. Sci.*, **39,** 2192–2210.

Mak, M., and P. R. Bannon, 1984: Frontogenesis in a moist semigeostrophic mode. *J. Atmos. Sci.*, **41,** 3485–3500.

Ogura, Y., and Y. L. Chen, 1977: A life history of an intense mesoscale convective storm in Oklahoma. *J. Atmos. Sci.*, **34,** 1458–1476.

——, and M. Liou, 1980: The structure of a midlatitude squall line: a case study. *J. Atmos. Sci.*, **37,** 553–567.

——, and Portix, 1982: Structure of the cold front observed in SESAME-AVE III and its comparison with the Hoskins-Bretherton horizontal shear model. *J. Atmos. Sci.*, **39,** 1783–1802.

——, and Jiang, 1985: A Modelling Study of Heating and Drying Effects of Convection in an Extratropical Mesoscale Convective System. *J. Atmos. Sci.*, **42,** 2478–2492.

Orlanski, I., 1986: Localized baroclinicity: A source for meso-cyclones. *J. Atmos. Sci.*, **43,** 2857–2885.

——, and B. B. Ross, 1977: The circulation associated with a cold front. Part 1: Dry case. *J. Atmos. Sci.*, **34,** 1619–1633.

——, B. B. Ross, L. Polinsky and R. Shaginaw, 1985: Advances in the theory of atmospheric fronts. *Adv. Geophys.*, **28B,** 223–252.

Orville, H. D., Y. H. Kuo, R. D. Farley and C. S. Hwang, 1980: Numerical simulation of cloud interactions. *J. Rech. Atmos.*, **14,** 499–516.

Palmen, E., and C. W. Newton, 1969: *Atmospheric Circulation Systems.* Academic Press.

Reeder, M. J., and R. K. Smith, 1986: A comparison between frontogenesis in the two-dimensional Eady-model of baroclinic instability and summertime cold fronts in the Australian region. *Quart. J. Roy. Meteor. Soc.*, 112.

Ross, B., and I. Orlanski, 1978: The circulation associated with a cold front. Part II: Moist Case. *J. Atmos. Sci.*, **35,** 445–465.

Ryan, B. F., and K. J. Wilson, 1985: The Australian summertime cool change. Part III: Subsynoptic and mesoscale model. *Mon. Wea. Rev.*, **113,** 224–240.

Sanders, F., 1955: An investigation of the structure and dynamics of an intense surface frontal zone. *J. Meteor.*, **12,** 542–552.